

1 **Hydrothermal upgrading as an important tool for the REE mineralization in the**
2 **Miaoya carbonatite-syenite complex, Central China**

3

4 **Word Count: 9468 Revision 2**

5

6 **RONG-LIN MA^{1,2}, WEI TERRY CHEN^{1,2,*}, WEI ZHANG¹, AND YOU-WEI**
7 **CHEN¹**

8

9 1 State key Laboratory of Ore Deposit Geochemistry, Institute of Geochemistry, Chinese
10 Academy of Sciences, Guiyang 550081, China

11 2 University of Chinese Academy of Sciences, Beijing 100049, China

12

13

14

15

16

17

18

19

20

21 Corresponding author: Wei Terry Chen (chenwei@mail.gyig.ac.cn)

22

ABSTRACT

23

24 Secondary hydrothermal reworking of REEs has been widely documented in
25 carbonatites/alkaline rocks, but its potential role in the REE mineralization associated
26 with these rocks is currently poorly understood. This study conducted a combined
27 textural and in-situ chemical investigation on the REE mineralization in the ~430 Ma
28 Miaoya carbonatite-syenite complex, central China. Our study shows that the REE
29 mineralization, dated at ~220 Ma, is characterized by a close association of REE minerals
30 (monazite and/or bastnäsite) with pervasive carbonatization overprinting the carbonatites
31 and syenites. In these carbonatites and syenites, both the apatite and calcite, which are the
32 dominant magmatic REE-bearing minerals, exhibit complicated internal textures that are
33 generally composed of BSE-bright and BSE-dark domains. Under BSE imaging, the
34 former domains are homogeneous and free of pores or mineral inclusions, whereas the
35 latter have a high porosity and inclusions of monazite and/or bastnäsite. In-situ chemical
36 analyses show that the BSE-dark domains of the apatite and calcite have light REE
37 concentrations and $(La/Yb)_N$ values much lower than the BSE-bright areas. These
38 features are similar to those observed in metasomatized apatite from mineral-fluid
39 reaction experiments, thus indicating that the BSE-dark domains formed from primary
40 precursors (i.e. represented by the BSE-bright domains) through a fluid-aid,
41 dissolution-reprecipitation process during which the primary light REEs are
42 hydrothermally remobilized. New, *in-situ* Sr-Nd isotopic results of apatite and various

43 REE minerals, in combination with mass balance calculations, strongly suggest that the
44 remobilized REEs are responsible for the subsequent hydrothermal REE mineralization in
45 the Miaoya complex. Investigations of fluid inclusions show that the fluids responsible
46 for the REE mobilization and mineralization are CO₂-rich, with medium temperatures
47 (227-340 °C) and low salinities (1.42-8.82 wt%). Such a feature, in combination with
48 C-O isotopic data, indicates that the causative fluids are likely co-genetic with fluids from
49 coeval orogenic Au-Ag deposits (220-200 Ma) in the same tectonic unit. Our new
50 findings provide a strong evidence that the late hydrothermal upgrading of early
51 cumulated REEs under certain conditions could also be an important tool for REE
52 mineralization in carbonatites, particularly for those present in convergent belts where
53 faults (facilitating fluid migration) and hydrothermal fluids are extensively developed.

54

55 **Keywords:** Apatite, Calcite, REE mobilization and mineralization, hydrothermal
56 upgrading, Miaoya carbonatite-syenite complex

57

58

INTRODUCTION

59

60 Carbonatites and/or associated alkaline rocks have been important providers of REEs,
61 particular the light REEs (Mariano, 1989; Sheard et al., 2012), thus are important
62 exploration targets. Although there are more than 500 occurrences of carbonatites in the
63 world and most of them contain elevated concentrations of REEs, only a few display

64 economic potential to warrant exploitation (Woolley and Kjarsgaard, 2008; Verplanck et
65 al., 2016). Hence, unveiling key factors or processes leading to economic concentrations
66 of REEs in these rocks have long been an attractive topic for ore genesis studies over the
67 past decades (Xie et al., 2009; Pandur et al., 2014; Hou et al., 2015; Smith et al., 2016;
68 Song et al., 2018). It was commonly accepted that processes responsible for REE
69 enrichment in these rocks include primary magmatic concentration (e.g. the Mountain
70 Pass deposit, California, USA) (Castor, 2008), enrichment in lately exsolved fluids
71 through extreme fractionation of the carbonatitic or alkaline magmas, e.g. the
72 Maoniuping deposit, SW China (Xie et al., 2009; Hou et al., 2015; Liu and Hou, 2017),
73 or a combination of the processes mentioned above (Pandur et al., 2014; Broom-Fendley
74 et al., 2016). There is also increasing evidence showing that hydrothermal redistribution
75 of REEs cumulated in early carbonatites or alkaline rocks, triggered by late autogenetic
76 or external fluids, is also responsible for local REE enrichments, e.g. the Thor Lake and
77 Strange Lake deposits, Canada (Salvi and Williams-Jones, 1996; Sheard et al., 2012; Gysi
78 and Williams-Jones, 2013; Cheng et al., 2018; Cangelosi et al., 2020). However, the
79 potential contributions of the hydrothermal reworking to REE mineralization in such
80 kinds of deposits are still far from being clearly understood. Particularly, this unresolved
81 issue likely gives rise to the controversies regarding ore genesis of some
82 carbonatite-related REE deposits that show clear evidence of late hydrothermal overprints.
83 A notable example could be the world largest Bayan Obo REE-Nb-Fe deposit where
84 primary mineralogy and textures were overprinted by multiple hydrothermal events

85 (Smith et al., 2015; and reference therein). In this deposit, late hydrothermal fluids
86 (millions of years younger than the carbonatites) were suggested to be the key for major
87 REE mineralization (Ling et al., 2013; Yang et al., 2017), whereas others proposed that
88 the early carbonatitic magmatism played a key role (Yang et al., 2019).

89 The REE mineralization in the ~430 Ma Miaoya carbonatite-syenite complex, central
90 China is an ideal research target for evaluating the role of late hydrothermal
91 metasomatism on REE mineralization in carbonatites and/or alkaline rocks. Although not
92 mined currently, the potential REE reserve in the Miaoya complex was estimated to be
93 1.21 Mt. REE₂O₃ @ 1.5 wt% (Qian and Li, 1996). The REE mineralization was
94 confirmed to be hydrothermal origin and is spatially restricted to the complex, but direct
95 U-Pb dating of REE minerals obtained much younger ages of 230-210 Ma (Xu et al.,
96 2014; Ying et al., 2017; Zhang et al., 2019a). As such, few studies have suggested that the
97 younger REE minerals could have formed from secondary remobilization of early REE
98 mineralization (Ying et al., 2017, 2020; Zhang et al., 2019a, 2019b) or precipitated from
99 external REE-rich fluids that overprinted the complex (Cimen et al., 2018). However, the
100 reliability of these interpretations cannot be evaluated, as most of the data were obtained
101 by analyses of bulk ore/rocks or minerals separates containing multiple generations of
102 components (Ying et al., 2017, 2020; Cimen et al., 2018; Zhang et al., 2019a, 2019b).
103 Moreover the nature and sources of the causative fluids has not comprehensively been
104 discussed.

105 In this study, we described the styles of the REE mineralization in the Miaoya complex

106 in detail with emphases on the textural relationships of REE minerals with other
107 hydrothermal minerals and the internal features of various rock/ore-forming minerals, in
108 order to re-establish the paragenetic sequence of the complex and associated
109 mineralization/alteration. Moreover, utilizing electron microprobe (EMP) analysis, laser
110 ablation inductively coupled plasma mass spectrometry (LA-ICPMS), and laser ablation
111 multi-collector inductively coupled mass spectrometer (LA-MC-ICP-MS) techniques, we
112 have obtained *in-situ* major-trace elemental and Sr-Nd isotopic compositions of various
113 minerals forming during magmatic (e.g. apatite and calcite) and hydrothermal (e.g.
114 monazite and bastnäsite) stages. The new dataset, together with mass balance calculations
115 based on compositions of altered apatite/calcite and unaltered counterparts, allows us to
116 explore mobilization and mass transfer of REEs during fluids metasomatism, and thus in
117 turn convincingly constrain the sources of REEs and the relative roles of early magmatic
118 and late hydrothermal processes on the REE mineralization. In addition, Raman
119 spectroscopic and microthermometric analyses were conducted to constrain the nature
120 and potential sources of the fluids responsible for the REE mobilization and
121 mineralization.

122

123

GEOLOGICAL BACKGROUND

124

125 The Qinling Orogenic Belt, extending east-west nearly 2500 km across Central China,
126 is bounded by the North China Block to the north and the Yangtze Block to the south

127 along the Sanbao and Longmenshan-Dabashan faults, respectively (Meng and Zhang,
128 2000; Ratschbacher, 2003; Dong et al., 2011; Fig. 1a). The belt comprises four units
129 separated by the Luanchuan, Shangdan and Mianlue faults from north southward,
130 including the Southern North China Block, North Qinling unit, South Qinling unit, and
131 Northern South China Block (Fig. 1b). Formation of the orogenic belt involved the
132 collision of North Qinling and South Qinling units during the Carboniferous and the final
133 collision of the North China Craton and South China Craton during the Triassic (230-220
134 Ma) (Meng and Zhang, 2000; Wu and Zheng, 2013; Dong and Santosh, 2016).

135 The South Qinling unit, where the Miaoya carbonatite-syenite complex is located, is
136 comprised of a Precambrian basement covered by a 12 km-thick sedimentary sequence
137 Neoproterozoic to Triassic in age (Dong et al., 2011). The basement rocks are dominated
138 by the Douling and Xiaomoling complexes in the north and the Wudang and Yaolinghe
139 Groups in the south. The Neoproterozoic to Triassic cover sequences include the strongly
140 folded Sinian platform-type carbonate and clastic rocks, Cambrian-Ordovician limestones,
141 Silurian shales, Devonian to Carboniferous clastic rocks with interlayered limestone, and
142 Permian-Triassic sandstones (Mattauer et al., 1985; Ratschbacher et al., 2003; Dong et al.,
143 2011; Wu and Zheng, 2013; Liu et al., 2016). Silurian magmatism is widespread in this
144 region, including ca. 430 Ma mafic-ultramafic dykes, volcanic rocks, and
145 carbonatite-syenite complexes (e.g., Shaxiongdong and Miaoya) (Zhang et al. 2007; Xu
146 et al. 2008). There are also few early Mesozoic granitoids (250 to 190 Ma) randomly
147 distributed in this belt (Xiao et al., 2017; Fig. 1b).

148

149

REE MINERALIZATION IN THE MIAOYA COMPLEX

150

151 The Miaoya complex is located in the southwestern margin of the Wudang Terrane in
152 the South Qinling unit (Fig. 1b), covering an area of 6.5 km². It intruded the meta-quartz
153 keratophyre of the Neoproterozoic Yaolinghe Group and the schist of the Late Silurian
154 Meiziya Group along the Ankang-Desheng-Fangxian fault (Fig. 1c). The complex is
155 composed mainly of syenites (90 %) and carbonatites (7.5 %), with xenoliths of country
156 rocks (2.5 %) mostly present in the margins (Figs. 1c and 2a-2c). The syenites are
157 composed dominantly of K-feldspar (70 vol%) with subordinate but variable amounts of
158 calcite (12 vol%), albite (10 vol%), apatite (1 vol%), zircon, Nb-bearing minerals (e.g.
159 pyrochlore and columbite), and Fe-Ti oxides (e.g. ilmenite, magnetite and rutile) (Fig.
160 2f). The carbonatites are generally present as stocks and/or dykes intruding the syenites
161 (Figs. 1c and 2a), and can be classified as calciocarbonatites (>95%) and
162 ferrocarbonatites (<5%) in terms of different mineral assemblages (Su et al., 2019). The
163 calciocarbonatites are composed mainly of fine- to medium-grained calcite (0.1 to 2 mm)
164 (85 vol%) and subordinate apatite (~9.5 vol%) with trace amounts of monazite, bastnäsité,
165 parasite, allanite, K-feldspar, albite, quartz, biotite, zircon, Nb-bearing minerals (e.g.
166 pyrochlore and columbite), and Fe-Ti oxides (e.g. ilmenite, magnetite and rutile) (Fig.
167 2g). In contrast, the ferrocarbonatites are dominated by fine-grained ankerite (5-20 µm)
168 (>70 vol%) with subordinate calcite (~10 vol%), bastnäsité (~5 vol%), and monazite (~2

169 vol%) and trace amounts of parisite, fluorite, and sulfides (Fig. 3f). Xu et al. (2014) has
170 obtained zircon ages of 766 Ma for the syenites, but such ages were suggested to be
171 unreliable by Zhu et al. (2016) and Ying et al. (2017) who both obtained a similar zircon
172 age of 440 Ma for the syenites. Considering that an age of 766 Ma is comparable to those
173 of the country rocks (i.e. volcanic rocks of the Yaolinghe Group), we speculated that the
174 so-called “syenites” samples in Xu et al. (2014) could be xenoliths of the country rocks
175 (particularly that the Miaoya complex contains 2.5 vol% xenoliths). For the carbonatites,
176 Zhu et al. (2016) and Ying et al. (2017) obtained similar zircon ages of ~430 Ma. This
177 age should be reliable as these zircon grains are characterized by low U and high Th/U
178 ratios, similar to zircons crystallized from carbonatitic magmas (Yuan et al., 2008). These
179 results indicate that both the carbonatite and syenites are broadly coeval and formed at
180 around 440 to 430 Ma.

181 Both the carbonatites and syenites have undergone extensive carbonatization that is
182 characterized by the presence of secondary, fine-grained calcite, ankerite, dolomite,
183 quartz and minor chlorite and Fe-oxides, which replace early carbonatite and syenite
184 assemblages (e.g. calcite, K-feldspar or apatite) (Figs. 2f, 2g, 3a, and 3b). The
185 carbonatization is also associated with the formation of abundant carbonate-rich veinlets
186 composed dominantly of calcite, dolomite, and/or quartz (Figs. 2d, 2e, 2h, and 2i).

187 The REE mineralization in the complex, dated at 230 to 210 Ma, is closely associated
188 with the carbonatization, pervasively overprinting both the carbonatites and syenites as
189 disseminated REE minerals or as REE mineral-rich veinlets or stockworks (Fig. 2e). As

190 such, the REE ores are essentially REE-mineralized syenites and carbonatites (Liu et al.,
191 1984), such that there are no clear boundaries between the REE ores and hosting syenites
192 or carbonatites (Figs. 2a and 2b). REE ore bodies were previously defined by these REE
193 concentrations, and most of the defined ore bodies are lentoid and located mostly in the
194 upper parts of the complex (Fig. 1d).

195 The REE minerals in the ores are dominated by monazite (20-300 μm), bastnäsité
196 (1-35 μm), and/or allanite (1-60 μm) (Fig. 3). Parisite is also locally present, commonly
197 replacing bastnäsité (Fig. 3h). The REE minerals are generally anhedral to subhedral, and
198 are closely intergrown with hydrothermal minerals typically including fine- to
199 medium-grained ankerite, calcite, sulfide, quartz, biotite, and phengite (Fig. 3). It is also
200 noteworthy that some of the monazite grains commonly show an intimate association
201 with relatively large apatite grains in both the syenites and carbonatites (Figs. 3a-3e). For
202 example, they are mostly present as fine inclusions (1-20 μm) enclosed in or as irregular
203 streaks distributed along fissures and margins of the apatite grains. These apatite grains,
204 as will be illustrated below, exhibit complicated internal textures under back scattered
205 electron (BSE) imagings.

206 On the basis of the macro- and micro- textural relationships of the mineral assemblages
207 described above, we establish a paragenetic sequence for the formation of the Miaoya
208 complex and subsequent REE mineralization, consisting of magmatic and hydrothermal
209 stages (Supplemental¹ Fig. 1). The early magmatic stage is characterized by the formation
210 of magmatic minerals in early syenites and slightly later carbonatites. This includes

211 dominantly K-feldspar and calcite, and subordinate apatite, albite, quartz, and biotite with
212 trace amounts of REE minerals such as monazite and allanite (Figs. 2f and 2g) (Zhang et
213 al., 2019a). The late hydrothermal stage is characterized by the formation of abundant
214 REE minerals (monazite, bastnäsite, allanite and parisite) associated with pervasive
215 carbonatization and variable amounts of calcite, K-feldspar, quartz, fluorite, dolomite,
216 chlorite, and phengite (Fig. 3).

217

218 **INTERNAL TEXTURES OF APATITE AND CALCITE**

219

220 Detailed textural relationships between apatite and calcite were further investigated by
221 scanning electron microscopy – cathode luminescence (SEM-CL). Detailed analytical
222 methods are provided in Supplemental¹ Method.

223

224 **Texture of apatite**

225 Apatite grains in the carbonatites and syenites are broadly similar in terms of internal
226 textures (Figs. 3a-3e). Under BSE imaging, these grains are generally composed of
227 several domains with variable BSE intensities (Figs. 3b-3e). In most cases, these textures
228 consist of only two parts consisting of BSE-bright and BSE-dark domains (Figs. 3d and
229 3e), but in rare cases they may consist of three parts named as BSE-bright, BSE-dark-I,
230 and BSE-dark-II domains of which this last domain is darkest under BSE imaging (Fig.
231 3c). The contacts among different domains in each apatite grain are generally irregular

232 and sharp (Figs. 3c-3e). The BSE-bright domains are commonly homogeneous without
233 any cracks, and are present mostly in the centers of the apatite grains (Fig. 3c). In contrast,
234 the BSE-dark domains, including I and II, are mostly present along the margins of the
235 apatite grains, and are irregular, cracks-developed and rich in pores, cracks, and mineral
236 inclusions. Notably, the BSE-dark-II domains, if present, occur as irregular strips and
237 patches embaying both the BSE-bright and BSE-dark-I domains (Fig. 3c).

238 The apatite grains are closely associated with fine-grained REE minerals dominated by
239 monazite with minor bastnäsite (Fig. 3). These REE minerals are either present as fine
240 inclusions enclosed in the BSE-dark domains or as anhedral grains distributed along the
241 apatite grain rim (Figs. 3a-3e) where calcite and sulfide inclusions are also commonly
242 present. In the latter case, the REE minerals are relatively large, subrounded to angular in
243 shape, and are generally homogenous even under high-resolution BSE imagings (Fig.
244 3d).

245

246 **Texture of calcite**

247 Calcite is the predominant mineral of the calciocarbonatites in the Miaoya complex,
248 and is commonly present as subhedral to anhedral grains with grain sizes highly variable
249 (0.1 to 2 mm) (Fig. 2g). Similar to the apatite, the calcite also shows complex internal
250 textures that are composed of BSE-bright and BSE-dark domains under high-contrast
251 BSE imaging (Fig. 3k). The BSE-bright domains are generally homogeneous and free of
252 inclusions or voids, whereas the BSE-dark domains contain abundant voids and mineral

253 inclusions dominated by fine-grained REE minerals, e.g., monazite, bastnäsite, and/or
254 parisite, and minor pyrite, celestite, barite, and strontianite (Fig. 3k).

255

256

MINERAL CHEMISTRY

257 Major and trace elemental compositions of different minerals were obtained by EMP
258 analytical and LA-ICPMS techniques, respectively. Analytical methods and results are
259 available in Supplemental¹ Method and Supplemental¹ Table S1-S5, respectively.

260

261 **Apatite chemistry**

262 Apatite grains in the altered carbonatites and syenites, including both the BSE-bright
263 and BSE-dark domains, are all fluorapatite characterized by high F (3.04-4.79 wt%) but
264 low Cl or OH contents (<0.02 wt%) (Fig. 4a; Supplemental¹ Table S1). The BSE-bright
265 domains have CaO (52.40-54.72 wt%) slightly lower than the BSE-dark-I and II domains
266 (53.42-56.52 wt%), whereas the P₂O₅ contents in different domains are broadly similar
267 (Figs. 7a-7c). In terms of trace elements, LA-ICP-MS analyses show that the BSE-bright
268 domains have mean Sr (12647 ppm), Na (2095 ppm), Ga (86 ppm), Ge (40 ppm), Ba (18
269 ppm), and Zr (21 ppm) values remarkably higher than BSE-dark-I and II domains
270 (Supplemental¹ Table S2). Such chemical differences among different domains are also
271 clearly revealed by the EMP mapping (Fig. 7).

272 In terms of REE concentrations, LA-ICP-MS analyses indicate that all the domains are
273 similarly enriched in LREEs relative to HREEs (Fig. 4i), but exhibit dramatically

274 different REE contents and chondrite-normalized REE patterns (Figs. 4 and 5). The
275 BSE-bright domains have the highest REEs (total: 7778-16525 ppm), followed by the
276 BSE-dark-I (5845-10287 ppm) and BSE-dark-II domains (1048-4742 ppm)
277 (Supplemental¹ Table S2). Notably, total contents of REE+Y in all the domains are
278 positively correlated with Na and Sr, but do not exhibit a clear correlation with Si (Figs.
279 4b, 4c and 4e). Moreover, there is a negative correlation between REE+Y+Na and Ca
280 (Fig. 4d). In the chondrite-normalized REE diagrams, both the BSE-bright and
281 BSE-dark-I domains exhibit smoothly, right-dipping REE patterns (Figs. 5a and 5b), even
282 though the BSE-bright domains tend to have relatively high LREE contents, $(La/Yb)_N$
283 and $(La/Nd)_N$ values (Figs. 4g and 4h). In contrast, the BSE-dark-II domains exhibit
284 distinctly inverted “U”-like REE patterns in which the LREE portions are almost flat,
285 corresponding to much lower values of $(La/Yb)_N$ (4.8-74.6) and $(La/Nd)_N$ (0.4-2.3) (Fig.
286 5c; Supplemental¹ Table S2). Instead, the HREE patterns are broadly parallel to those of
287 the BSE-bright and BSE-dark-I domains (Fig. 5). All the domains have undistinguishable
288 Eu anomalies with δEu values varying from 0.87 to 1.22.

289

290 **Calcite chemistry**

291 Both the BSE-bright and BSE-dark domains of the calcite are analysed. The results
292 show that the former has CaO (52.75-55.05 wt%) and REE (240-370 ppm) higher but Na
293 (44.1-64.4 ppm), Mg (910-2346 ppm), Mn (1688-5018 ppm), and Fe (3350-14204 ppm)
294 lower than the latter (Figs. 6a and 6b; Supplemental¹ Table S3 and S4). In total, both

295 domains have comparable Sr contents but in the case of an individual calcite grain, the
296 BSE-bright domain tends to have relatively high Sr. Both domains exhibit similarly
297 LREE-enriched, right-dipping chondrite-normalized REE patterns, but the BSE-dark
298 domains have relatively low LREE contents and (La/Yb)_N ratios (Fig. 6c), which is
299 particularly remarkable for an individual calcite. In contrast, both domains have similar
300 HREE concentrations and exhibit similarly positive Eu anomalies with δEu varying from
301 1.06 to 1.34 (Supplemental¹ Fig. 2).

302

303 **Phengite and chlorite chemistry**

304 Both phengite and chlorite from the late hydrothermal stage were analyzed for major
305 elemental compositions. The phengite grains are F-rich (0.12-1.18 wt%) (Supplemental¹
306 Table S5), and have limit variations of K₂O (10.34-10.94 wt%), SiO₂ (48.77-51.99 wt%),
307 Al₂O₃ (26.69-31.84 wt%), MgO (1.42-3.33 wt%), and FeO (3.15-4.18 wt%). The chlorite
308 grains have much lower F and Cl (both <0.02 wt%) (Supplemental¹ Table S5), and
309 exhibit relatively large variations in SiO₂ (22.77-25.03 wt%), Al₂O₃ (18.95-23.39 wt%),
310 MgO (5.07-11.46 wt%), and FeO (28.76-38.52 wt%).

311

312 ***IN-SITU* SR AND ND ISOTOPES OF MINERALS**

313 Detailed methods for *in-situ* Sr-Nd isotopic analyses of apatite, monazite, and
314 bastnäsite are provided in the Supplemental¹ Method, and the results are given in
315 Supplemental¹ table S6-S9.

316

317 **Sr-Nd isotopes of apatite**

318 All the domains have extremely low $^{87}\text{Rb}/^{87}\text{Sr}$, consistent with their low Rb but high Sr
319 concentrations (Supplemental¹ Table S2). The $^{87}\text{Sr}/^{86}\text{Sr}$ ratios of the BSE-bright domains
320 in apatite range from 0.70360 to 0.70389, which are broadly identical to those of the
321 BSE-dark domains (I and II) (Fig. 8; Supplemental¹ Table S6). In addition, the
322 BSE-bright domains have $^{147}\text{Sm}/^{144}\text{Nd}$ and $^{143}\text{Nd}/^{144}\text{Nd}$ ratios ranging from 0.09064 to
323 0.10809 and 0.51227 to 0.51251, respectively, similar to those of the BSE-dark-I domains,
324 but slightly lower than those of the BSE-dark-II domains with $^{147}\text{Sm}/^{144}\text{Nd}$ and
325 $^{143}\text{Nd}/^{144}\text{Nd}$ varying from 0.10600 to 0.25732 and 0.51243 to 0.51263, respectively,
326 (Supplemental¹ Table S7). On the basis of the obtained ages of ~220 Ma for the REE
327 minerals (Xu et al., 2014; Ying et al., 2017, Zhang et al., 2019a), we calculated the $\epsilon_{\text{Nd}}(t)$
328 values, by using the formula of $[(^{143}\text{Nd}/^{144}\text{Nd})_{\text{sample}}(t) / (^{143}\text{Nd}/^{144}\text{Nd})_{\text{CHUR}}(t) - 1] \times$
329 10000, for different domains in the apatite grains. The results show that the $\epsilon_{\text{Nd}}(t)$ values
330 of the BSE-bright domains range from -4.58 to 0.03, broadly comparable to those of the
331 BSE-dark-I (-3.66 to 0.19) and BSE-dark-II (-4.63 to 0.36) domains (Fig. 9a).

332

333 **Nd isotopes of monazite and bastnäsite**

334 Three types of monazite grains, including those associated with apatite, those
335 occurring as a dissemination, and those in veinlets, were selected for *in-situ* Nd isotopic
336 analyses. The monazite grains associated with apatite, including those inside and outside

337 the apatite hosts, have similar $^{147}\text{Sm}/^{144}\text{Nd}$ and $^{143}\text{Nd}/^{144}\text{Nd}$ ratios ranging from 0.05674
338 to 0.08416 and 0.51240 to 0.51247, respectively. These ratios are broadly identical to
339 those of the monazite grains in the dissemination and veinlets (Supplemental¹ Table S8).
340 Using the age of ~220 Ma, the calculated $\epsilon_{\text{Nd}}(t)$ values for the monazite associated with
341 apatite have a limited variation (-1.18 to 0.30) that are undistinguishable from those of
342 the monazite in disseminations (-2.03 to -0.27) and veinlets (-1.23 to -0.06) (Fig. 9b).

343 Bastnäsite grains, as disseminations and in veinlets, have similarly limited variations of
344 $^{147}\text{Sm}/^{144}\text{Nd}$ (0.06639-0.09764) and $^{143}\text{Nd}/^{144}\text{Nd}$ (0.51238-0.51249), corresponding to the
345 calculated $\epsilon_{\text{Nd}}(t)$ values ($t=220$ Ma) ranging from -0.52 to 0.50 and -1.70 to -0.23,
346 respectively (Supplemental¹ Table S9; Fig. 9c). Such $\epsilon_{\text{Nd}}(t)$ values are also comparable to
347 those of the monazite from the diverse types mentioned above.

348

349 **FLUID INCLUSION MICROTHERMOMETRY AND RAMAN SPECTROSCOPE**

350 Fluid inclusions in the apatite BSE-dark domains were investigated to understand the
351 nature of the late hydrothermal fluids (Fig. 10a). Detailed methods for
352 microthermometric and Raman spectroscopic analyses of the fluid inclusions are
353 provided in Supplemental¹ Method. The fluid inclusions are elliptical or irregular in
354 shape, with sizes ranging from 2 to 8 μm (Figs. 10b and 10c). They are commonly
355 two-phase, liquid-rich inclusions with the vapor bubbles occupying 8-37 vol% (Figs.
356 10-10c). Raman spectroscopic analyses show that there are two peaks around 1284 cm^{-1}

357 and 1387 cm^{-1} , indicating that CO_2 is the major vapor phase (Fig. 10d). Most of the fluid
358 inclusions were observed to contain a clathrate, which decomposed at 5.1 to 9.3 $^{\circ}\text{C}$,
359 corresponding to salinities of 1.42 to 8.82 wt% NaCl equiv. (Fig. 10f) and
360 homogenization temperatures of 226 to 340 $^{\circ}\text{C}$ (Fig. 10e; Supplemental¹ Table S10).

361

362

DISCUSSION

363

364 **Fluid-aided remobilization of early cumulated light REEs in the Miaoya complex**

365 Both apatite and calcite are the dominant primary magmatic, REE-bearing minerals in
366 the early carbonatites and/or syenites. Our textural observations show that the two
367 minerals exhibit similar internal textures that are characterized by the presence of several
368 domains with distinguishable appearances (Figs. 3a-3e). Similar textures, particularly the
369 monazite-bearing apatite, have been replicated in experiments involving mineral-fluid
370 interaction (Harlov et al., 2002b, 2005; Harlov and Föster, 2003). These textures have
371 also commonly been observed in some iron oxides-apatite and iron oxide copper-gold
372 deposits (Harlov et al., 2002a; Chen and Zhou, 2015; Li and Zhou, 2015; Zeng et al.,
373 2016). These textures have been demonstrated to form via a fluid-aided, coupled
374 dissolution-reprecipitation process during which the REEs have been hydrothermally
375 remobilized to form REE minerals such as monazite (Harlov et al., 2002a; Chen and
376 Zhou, 2015; Li and Zhou, 2015). In the case of Miaoya, the BSE-dark domains (including
377 both I and II) in the apatite and calcite host an abundant micro-porosity, fluid inclusions,

378 and mineral inclusions, compared to the BSE-bright domains that are homogeneous and
379 free of pores and mineral inclusions (Figs. 3b-3e). This feature indicates that the BSE
380 dark domains formed from the bright domains (original apatite) through fluid infiltration
381 and chemical alteration as observed in the experiments (e.g., Harlov et al., 2002a). It is
382 also notable that some of the apatite grains contain both BSE dark I and II domains (Figs.
383 3c-3e), indicating variable degrees of metasomatic alteration possibly related to
384 consecutive infiltration of fluids.

385 Both the BSE dark I and II domains in the apatite and the calcite grains have REE
386 concentrations that are lower than the BSE-bright domains, indicating that the REEs have
387 been extensively mobilized and leached from the original apatite during metasomatic
388 alteration. In particular, the BSE-dark domains are depleted in light REE, indicating that
389 the light REEs were more mobile than the heavy REEs which in many grains are only
390 slightly modified (Fig. 5). In addition to the light REEs, the BSE-dark domains in the
391 apatite are also depleted in Y, Na, and Sr relative to the BSE-bright domains (Fig. 7). It is
392 notable that REE+Y in these domains vary positively with Na and Sr but negatively with
393 Ca (Figs. 4c-4e), indicating that these elements were incorporated in the apatite through
394 the coupled substitution reaction: $\text{Na}^+ + (\text{REE} + \text{Y})^{3+} = 2\text{Ca}^{2+}$ and $\text{Sr}^{2+} = \text{Ca}^{2+}$ (Fig. 4d;
395 Roeder et al., 1987; Pan and Fleet, 2002; Harlov et al., 2002b, 2005; Harlov and Förster
396 2003). The leached REEs from the apatite and calcite were re-incorporated back into the
397 monazite inclusions and along the apatite grain rim (Fig. 3) (e.g., Harlov et al., 2002a), or
398 were partially transported outwards on scales of meters to be re-deposited as the REE

399 minerals present as disseminations or in veinlets.

400

401 **Remobilized REEs as the major contribution for the REE mineralization in Miaoya**

402 Although monazite or bastnäsite could have formed during the magmatic stage (Castor,
403 2008), our results confirm that the major REE mineralization in Miaoya is hydrothermal
404 in origin. For example, the REE minerals are present as a dissemination or in veinlets
405 where they closely associated with hydrothermal minerals (Fig. 3). The monazite grains
406 are characterized by low ThO₂ concentration (typically < 0.5 wt%, 0.29 wt% on average;
407 Xu et al., 2010), similar to typical hydrothermal monazite (Schandl and Gorton, 2004).
408 Available U-Pb dating of various monazite and bastnäsite have revealed consistent ages
409 of 230 to 210 Ma (Ying et al., 2017; Zhang et al., 2019a). This suggests that REE
410 mobilization and mineralization were coeval and related to a common fluid. However,
411 further evidence is needed to confirm if the major REE mineralization in Miaoya, which
412 occurs either as a dissemination or a veinlet, was also mainly contributed to by mobilized
413 REEs, even though most of the carbonatites and syenites in the Miaoya complex have
414 undergone pervasive carbonatization and extensive REE mineralization. To answer this
415 question, we conducted a comparison of Sr-Nd isotopic data from early apatite and REE
416 minerals in multiple stages and various occurrences. Mass balance calculations were also
417 conducted to confirm if the remobilized REEs are sufficient for the REE mineralization in
418 Miaoya.

419 **In-situ Sr-Nd isotopic constraints.** As the analyzed apatite grains have high Sr

420 (3637-17482 ppm) but extremely low Rb (<3.4 ppm), the measured $^{87}\text{Sr}/^{86}\text{Sr}$ ratios could
421 be used as initial $^{87}\text{Sr}/^{86}\text{Sr}$ ratios, without further age calibration. Our new results show
422 that the BSE-dark domains I and II in apatite have $^{87}\text{Sr}/^{86}\text{Sr}$ ratios and $\epsilon_{\text{Nd}}(t)$ values
423 similar to the primary apatite, i.e. BSE-bright domains (Figs. 8 and 9a), indicating that
424 the causative fluids do not contain enough Sr and Nd to sufficiently modify the initial Sr
425 and Nd isotopic ratios of the primary apatite, or else the fluids have Sr and Nd isotopic
426 compositions similar to the apatite precursors. The latter possibility, however, is unlikely,
427 since the newly obtained $\epsilon_{\text{Nd}}(t)$ values for monazite and bastnäsite in the altered apatite,
428 and as disseminations or veinlets (-2.03 to 0.50) are similar to those of the BSE-bright or
429 BSE-dark domains of the apatite, which ranges from -4.58 to 0.36 (Fig. 9). These features
430 strongly support the idea that REE mineralization in the Miaoya complex was sourced
431 mainly from early cumulated REEs in the magmatic carbonatites and syenites.

432 **Constraint of mass balance calculation.** In order to quantitatively evaluate the
433 overall mass transfer of REEs during remobilization, we also conducted mass balance
434 calculations for the altered apatite and calcite. Following the procedures of Li and Zhou
435 (2017), the calculations were made by assuming that Tm in apatite and Lu in calcite are
436 hydrothermally immobile. At the very beginning, the concentrations of Tm or Lu in the
437 altered domains of the apatite or calcite were normalized to those of the primary ones. On
438 this basis, other elements could be also normalized accordingly, and an enrichment factor
439 for a certain element could be calculated following the formula: $X_m = C_b / (\rho * C_a)$ (Li and
440 Zhou, 2017), in which X_m represents the enrichment factor of a certain element, while C_a

441 and C_b are the concentrations of certain element in the primary and altered domains,
442 respectively. The ρ values are the relative ratios of concentrations of immobile elements
443 (i.e. Tm and Lu) in the altered and primary domains, and were calculated to be 1.1 and
444 0.99 for Tm in apatite and Lu in calcite, respectively. The calculated enrichment factors
445 are provided in Supplemental¹ Table S11 and illustrated in Figure 11. In Figure 11, the
446 solid line for the enrichment factor as 1 defines no gain or loss. Departure from the line
447 defines gain (above the line) or loss (below the line) for a certain element. The calculated
448 results for apatite show that components lost include light REEs (La, Ce, Pr, Nd; 89.8%
449 lost), Na, Sr, Ba, Ga and Ge, whereas Mg, Al, Si, Zr, Nb, Th, U, Fe, and Mn were
450 variably enriched (Fig. 11a). On the other hand, components lost in calcite include
451 LREEs (La, Ce, Pr, Nd; 28.3% lost), P, Si, U, Ga, and Ge, whereas Na, K, Nb, Th, Sc,
452 and V are variably enriched (Fig. 11b).

453 On the basis of the calculated proportions of the LREE losses, we are able to estimate
454 the total amounts of remobilized LREEs from the primary apatite and calcite in the
455 Miaoya complex in order to confirm if it matches the reported REE reserve in Miaoya.
456 Detailed steps for the calculation are provided in Table 1. Firstly, we know that the
457 carbonatites stocks, which are mostly altered, cover a total area of about 0.49 km²
458 whereas the altered syenites cover a total area of about 5.85 km². Both rock types extend
459 to a depth of ~640 m below the current surface (Liu et al., 1984). As such, the total
460 volume of the carbonatites and the syenites are calculated to be 3.15×10^8 m³ and $3.76 \times$
461 10^9 m³, respectively (Table 1). Secondly, the total volumes of apatite and calcite in the

462 complex can be estimated on the basis of their contents in the carbonatites and syenites
463 (Table 1). On this basis, using a density ($\sim 3.19 \text{ ton/m}^3$) and the average LREE contents
464 (13660 ppm) for the primary apatite, along with the estimated proportions of LREE
465 losses (89.8%), the remobilized amounts of LREEs from the apatite in the carbonatites
466 and syenites were calculated to be 1.173 and 1.476 Mt, respectively (Table 1). On the
467 other hand, using the density ($\sim 2.71 \text{ ton/m}^3$) and average LREE contents (155 ppm) of
468 calcite, and the estimated proportions of LREE losses (28.3%), the remobilized amounts
469 of LREEs from calcite in the carbonatites and syenites were calculated to be 0.032 and
470 0.054 Mt, respectively (Table 1). As such, the total amount of remobilized LREEs can be
471 calculated to be 2.735 Mt (Table 1). Such a value is much higher than the reported
472 REE₂O₃ reserve of 1.21 Mt, which is only for those areas $> 1.2 \text{ wt}\%$ REE₂O₃ (Fig. 1d)
473 (Qian and Li, 1996). However, if those ores with grades ranging from 0.3 to 1.2 wt%
474 REE₂O₃ are incorporated (Fig. 1d), the total reserve, i.e. REE₂O₃ $> 0.3 \text{ wt}\%$, would be
475 much larger and could broadly match the estimated value of the mobilized LREEs (e.g.
476 Fig. 1d). Therefore, our mass balance calculation confirms that early cumulated LREEs,
477 which were mostly in the magmatic apatite and calcite from the complex, were sufficient
478 for the REE mineralization related to late hydrothermal reworking.

479

480 **Nature and potential sources of the causative fluids**

481 Results from the fluid inclusion study show that the causative fluids responsible for
482 REE remobilization and mineralization are CO₂-rich, with medium temperatures

483 (226-340 °C), and low salinities (1.42-8.82 wt%) (Fig. 10). The local presence of fluorite
484 and F-rich phengite in the mineralized veinlets imply that the fluids were also rich in F
485 (Supplemental¹ Table S5). All these ligands were well confirmed to be important
486 mediums aiding the mobility of REEs, particularly light REEs (Harlov et al., 2005;
487 Williams-Jones et al., 2012; Williams-Jones and Migdisov, 2014; Li et al., 2015; Perry
488 and Gysi, 2018). It is thus concluded that such low-salinity, CO₂-, F-, and Cl-rich fluids,
489 presumably unsaturated with REEs, should be responsible for REE mobilization and
490 subsequent mineralization in the Miaoya complex.

491 The potential sources of the causative fluids have not been addressed previously but
492 can be speculated about due to coeval, 230-210 Ma hydrothermal/mineralization events
493 in the same region. Available studies have revealed that numerous orogenic, 220 to 200
494 Ma Au-Ag deposits, e.g. Yindonggou, Xujiapo, Shejiayuan, Putang and Xunyang
495 deposits, are distributed along the South Qinling unit (Chen and Santosh, 2014). The
496 ore-forming fluids for these deposits were constrained to be CO₂-rich, with low to
497 medium temperatures and salinities (Feng et al., 1997; Cai et al., 1999; Pang et al., 2001;
498 Xu et al., 2012, 2018; Yue et al., 2013), which are broadly similar to the causative fluids
499 documented in Miaoya (Fig. 10). Moreover, a summary of previous C-O isotopic results
500 from the altered rocks/ores in the Miaoya complex shows that these data plot the field in
501 between the primary carbonatites and the Au-Ag deposits (Fig. 12) (Xu et al., 2014;
502 Cimen et al., 2018; Su et al., 2019; Zhang et al., 2019b). Such an isotopic feature strongly
503 indicates that the causative fluids are likely coeval and co-genetic with those of the

504 Au-Ag deposits in the same region.

505

506 **A genetic model for the REE mineralization in the Miaoya complex**

507 This study confirms that the formation of the Miaoya complex and associated REE
508 mineralization involved two separated stages. Both the syenites and carbonatites formed
509 from partial melting of the upper mantle under a rift setting at ~430 Ma (Xu et al., 2014;
510 Zhu et al., 2016; Su et al., 2019; Zhang et al., 2019a), likely followed by a combined
511 fractionation-immiscibility process (Fig. 13a; Su et al., 2019). It is noteworthy that
512 although both the carbonatites and syenites have elevated REE concentrations, our work
513 reveals that the REE-rich minerals formed in this stage were dominantly apatite with
514 minor monazite and/or bastnäsite (<1 vol%). Subsequent infiltration and overprinting by
515 external fluids during 230-210 Ma (Ying et al., 2017; Zhang et al., 2019a), possibly
516 co-genetic with the coeval orogenic Au-Ag mineralization in the same belt, pervasively
517 metasomatized the early carbonatites and syenites (Fig. 13b). Triggered by metasomatism,
518 the early cumulated REEs were extensively mobilized and transported on scales of meters
519 or even possibly tens of meters to be re-deposited as monazite and/or bastnäsite in the
520 form of disseminations or veinlets (Fig. 13c).

521

522

IMPLICATIONS

523

524 Numerous carbonatites and/or alkaline rocks are enriched in light REEs, but only few

525 contain sufficient amounts of REE minerals, here monazite and bastnäsite, for economic
526 exploitation. In most cases, the REEs in carbonatites are distributed in diverse minerals
527 (e.g. carbonates or apatite) that are generally not exploited. Our study provides a strong
528 evidence that secondary hydrothermal upgrading of early cumulated REEs under certain
529 conditions is the key for the REE mineralization, i.e. re-precipitation of economic REE
530 minerals, in the Miaoya complex. It could also be an also alternative important tool for
531 REE mineralization in other carbonatite-related deposits, such as the Bayan Obo. In
532 particular, our findings that the causative fluids for REE mineralization are co-genetically
533 related to the orogenic Au-Ag deposits formed during the final collision between the
534 North China and South China Cratons allow us to further speculate that hydrothermal
535 mobilization of REEs could be more widespread than previously documented,
536 particularly for REE deposits present in convergent belts where faults (facilitating fluid
537 migration) and hydrothermal fluids are generally more extensively developed. This
538 suggests that carbonatites and alkaline rocks (or even other REE-rich rocks) distributed in
539 the convergent belts could be potential targets for REE exploration.

540

541

ACKNOWLEDGMENTS

542 This study is supported by the National Key R&D Program of China
543 (2017YFC0602302) and Key Research Program of Frontier Sciences, CAS
544 (QYZDB-SSW-DQC008). This is also a contribution of National Natural Science
545 Foundation of China (41822303). We thank Lei Liu, Zhen-Dong Tian and Xiao-Wei Xie,

546 from the Institute of Geochemistry, Chinese Academy of Sciences, Yue-Heng Yang from
547 Institute of Geology and Geophysics, Chinese Academy of Sciences, Liang Li and Zi-Wei
548 Dong from Nanjing FocuMS Technology Co. Ltd. for the assistance during experimental
549 analyses. We are grateful to Cheng Xu and an anonymous reviewer for their constructive
550 comments, and Danial Harlov for handling the manuscript.

551

552

REFERENCES CITED

553 Broom-Fendley, S., Styles, M.T., Appleton, J.D., Gunn, G., and Wall, F. (2016) Evidence
554 for dissolution-reprecipitation of apatite and preferential LREE mobility in
555 carbonatite-derived late-stage hydrothermal processes. *American Mineralogist*, 101,
556 596-611.

557 Cai, J.H., Zhang, Y.M., and Fu, J.M. (1999) Study on fluid inclusion within quartz from
558 the Xujiapo gold-silver deposit, Northwest Hubei. *Geology Geology and Mineral
559 Resources of South China*, 4, 44-49.

560 Cangelosi, D., Broom-Fendley, S., Banks, D., Morgan, D., and Yardley, B. (2020) Light
561 rare earth element redistribution during hydrothermal alteration at the Okorusu
562 carbonatite complex, Namibia. *Mineralogical Magazine*, 84, 49-64.

563 Castor, S. (2008) The Mountain Pass rare-earth carbonatite and associated untrapotassic
564 rocks, California. *The Canadian Mineralogist*, 46, 779-806.

565 Chen, Y.J., and Santosh, M. (2014) Triassic tectonics and mineral systems in the Qinling
566 Orogen, central China. *Geological Journal*, 49, 338-358.

- 567 Chen, W.T., and Zhou, M.F. (2015) Mineralogical and geochemical constraints on
568 mobilization and mineralization of rare Earth elements in the Lala Fe-Cu-(Mo, Ree)
569 deposit, SW China. *American Journal of Science*, 315, 671-711.
- 570 Cheng, Z.G., Zhang, Z.C., Aibai, a., Kong, W.L., and Holtz, F. (2018) The role of
571 magmatic and post-magmatic hydrothermal processes on rare-earth element
572 mineralization: A study of the Bachu carbonatites from the Tarim Large Igneous
573 Province, NW China. *Lithos*, 314-315, 71-87.
- 574 Cimen, O., Kuebler, C., Monaco, B., Simonetti, S.S., Corcoran, L., Chen, W., and
575 Simonetti, A. (2018) Boron, carbon, oxygen and radiogenic isotope investigation of
576 carbonatite from the Miaoya complex, Central China: evidences for late-stage REE
577 hydrothermal event and mantle source heterogeneity. *Lithos*, 322, 225-237.
- 578 Demény, A., Ahijado, A., Casillas, R., and Vennemann, T.W. (1998) Crustal
579 contamination and fluid/rock interaction in the carbonatites of Fuerteventura
580 (Canary Islands, Spain): a C, O, H isotope study. *Lithos*, 44, 101-115.
- 581 Dong, Y.P., and Santosh, M. (2016) Tectonic architecture and multiple orogeny of the
582 Qinling Orogenic Belt, Central China. *Gondwana Research*, 29, 1-40.
- 583 Dong, Y.P., Zhang, G.W., Neubauer, F., Liu, X.M., Genser, J., and Hauzenberger, C.
584 (2011) Tectonic evolution of the Qinling orogen, China: review and synthesis.
585 *Journal of Asian Earth Sciences*, 41, 213-237.
- 586 Feng, J.Z., Wang, S.L., Ai, X., and Liu, K.M. (1997) Mineralizing physical-chemical
587 condition and fluid evolution in Maotang and Putang gold deposits, Henan. *Gold*

- 588 Geology, 3, 17-22 (in Chinese).
- 589 Gysi, A.P., and Williams-Jones, A.E. (2013) Hydrothermal mobilization of
590 pegmatite-hosted REE and Zr at Strange Lake, Canada: A reaction path model.
591 *Geochimica et Cosmochimica Acta*, 122, 324-352.
- 592 Harlov, D.E., and Förster, H.J. (2003) Fluid-induced nucleation of (Y+REE)-phosphate
593 minerals within apatite: nature and experiment. Part II. Fluorapatite. *American*
594 *Mineralogist*, 88, 1209-1229.
- 595 Harlov, D.E., Andersson, U.B., Förster, H.J., Nyström, J.O., Dulski, P., and Broman, C.
596 (2002a) Apatite-monzite relations in the Kiirunavaara magnetiteapatite ore,
597 northern Sweden. *Chemical Geology*, 191, 47-72.
- 598 Harlov, D.E., Förster, H.J., and Nijland, T.G. (2002b) Fluid-induced nucleation of
599 (Y+REE)-phosphate minerals within apatite: nature and experiment. Part I.
600 Chlorapatite. *American Mineralogist*, 87, 245-261.
- 601 Harlov, D.E., Wirth, R., and Förster, H. (2005) An experimental study of dissolution
602 reprecipitation in fluorapatite: Fluid infiltration and the formation of monazite.
603 *Contributions to Mineralogy and Petrology*, 150, 268-286.
- 604 Hou, Z.Q., Liu, Y., Tian, S.H., Yang, Z.M., and Xie, Y.L., (2015) Formation of
605 carbonatite-related giant rare-earth-element deposits by the recycling of marine
606 sediments. *Scientific Reports*, 5, 10231.
- 607 Li, X.C., and Zhou, M.F. (2015) Multiple stages of hydrothermal REE remobilization
608 recorded in fluorapatite in the Paleoproterozoic Yinachang Fe-Cu-(REE) deposit,

- 609 Southwest China. *Geochimica et Cosmochimica Acta*, 166, 53-73.
- 610 Li, X.C., and Zhou, M.F. (2017) Hydrothermal alteration of monazite-(Ce) and
611 chevkinite-(Ce) from the Sin Quyen Fe-Cu-LREE-Au deposit, northwestern
612 Vietnam. *American Mineralogist*, 102, 1525-1541.
- 613 Li, X.C., Zhao, X.F., Zhou, M.F., Chen, W.T., and Chu, Z.Y. (2015) Fluid inclusion and
614 isotopic constraints on the origin of the Paleoproterozoic Yinachang Fe-Cu-(REE)
615 deposit, southwest China. *Economic Geology*, 110, 1339-1369.
- 616 Ling, M.X., Liu, Y.L., Williams, I.S., Teng, F.Z., Yang, X.Y., Ding, X., Wei, G.J., Xie,
617 L.H., Deng, W.F., and Sun, W.D. (2013) Formation of the world's largest REE
618 deposit through protracted fluxing of carbonatite by subduction-derived fluids.
619 *Scientific Reports*, 3, 1-8.
- 620 Liu, Y., and Hou, Z.Q., (2017) A synthesis of mineralization styles with an integrated
621 genetic model of carbonatite-syenite-hosted REE deposits in the Cenozoic
622 Mianning-Dechang REE metallogenic belt, the eastern Tibetan Plateau,
623 southwestern China. *Journal of Asian Earth Sciences*, 2017, 137, 35-79.
- 624 Liu, J.Y., Li, S., Hao, Y.W., Zhu, H.M., and Li, G.P. (1984) A study on the carbonatite
625 type Nb-REE ore deposit of Miaoya, Hubei, China, 143 p, Monograph on mineral
626 deposit, Hubei (in Chinese).
- 627 Liu L., Liao X.Y., Wang Y.W, Wang C., Santosh M., Yang M., Zhang C.L., and Chen D.L.
628 (2016) Early Paleozoic tectonic evolution of the North Qinling Orogenic Belt in
629 Central China: insights on continental deep subduction and multiphase exhumation.

- 630 Earth Science Reviews, 159, 58-81.
- 631 Mariano, A.N. (1989) Economic geology of rare earth elements. In Geochemistry and
632 Mineralogy of Rare Earth Elements (B.R. Lipin & G.A. McKay, eds.). Reviews in
633 Mineralogy, 21, 309-337.
- 634 Mattauer, M., Matte, P., Malavieille, J., Tapponnier, P., Maluski, H., Xu, Z.Q., Lu, Y.L.,
635 and Tang, Y.Q. (1985) Tectonics of the Qinling belt: build-up and evolution of
636 eastern Asia. Nature, 317, 496-500.
- 637 Meng, Q.R., and Zhang, G.W. (2000) Geologic framework and tectonic evolution of the
638 Qinling orogen, Central China. Tectonophysics, 323, 183-196.
- 639 Pan, Y.M., and Fleet, M.E. (2002) Compositions of the apatite-group minerals:
640 substitution mechanisms and controlling factors. Reviews in Mineralogy and
641 Geochemistry, 48, 13-49.
- 642 Pandur, K., Kontak, D.J., and Ansdell, K.M., (2014) Hydrothermal evolution in the
643 Hoidas Lake vein-type REE deposit, Saskatchewan, Canada: Constraints from fluid
644 inclusion microthermometry and evaporate mound analysis. The Canadian
645 Mineralogist, 52, 717-744.
- 646 Pang, Q.B., Jia, W.G., Han, Z.W., and Chen, S.W. (2001) The mineralization conditions
647 for the Hg-Sb-Au deposits in Xunyang district, Shangxi Province. Geology and
648 Resources, 10, 91-101 (in Chinese).
- 649 Perry, E.P., and Gysi, A.P. (2018) Rare earth elements in mineral deposits: Speciation in
650 hydrothermal fluids and partitioning in calcite. Geofluids, 2018, 5382480.

- 651 Qian, D.D., and Li, J.Q. (1996) The discovering history of Chinese deposits: Hubei
652 volume, 177 p, Geological Publishing House, Beijing (in Chinese).
- 653 Ratschbacher, L., Hacker, B.R., Calvert, A., Webb, L.E., Grimmer, J.C., Mewilliams,
654 M.O., Ireland, T., Dong, S., and Hu, J. (2003) Tectonics of the Qinling (Central
655 China): tectonostratigraphy, geochronology, and deformation history.
656 Tectonophysics, 366, 1-53.
- 657 Roeder, P.L., MacArthur, D., Ma, X.-P., Palmer, G.R., and Mariano, A.N. (1987)
658 Cathodoluminescence and microprobe study of rare-earth elements in apatite.
659 American Mineralogist, 72, 801-811.
- 660 Salvi, S., and Williams-Jones, A.E. (1996) The role of hydrothermal processes in
661 concentrating HFSE in the Strange Lake peralkaline complex, northeastern Canada.
662 Geochimica et Cosmochimica Acta, 60, 1917-1932.
- 663 Schandl, E.S., and Gorton, M.P. (2004) A textural and geochemical guide to the
664 identification of hydrothermal monazite: criteria for selection of samples for dating
665 epigenetic hydrothermal ore deposits. Economic Geology, 99, 1027-1035.
- 666 Sheard, E.R., Williams-Jones, A.E., Heiligmann, M., Pederson, C., and Trueman, D.L.
667 (2012) Controls on the Concentration of Zirconium, Niobium, and the Rare Earth
668 Elements in the Thor Lake Rare Metal Deposit, Northwest Territories, Canada.
669 Economic Geology, 107, 81-104.
- 670 Smith, M.P., Campbell, L.S., and Kynicky, J. (2015) A review of the genesis of the world
671 class Bayan Obo Fe-REE-Nb deposits, Inner Mongolia, China: Multistage processes

- 672 and outstanding questions. *Ore Geology Reviews*, 64, 459-476.
- 673 Smith, M.P., Moore, K., Kavecsánszki, D., Finch, A.A., Kynicky, J. and Wall, F. (2016)
- 674 From mantle to critical zone: A review of large and giant sized deposits of the rare
- 675 earth elements. *Geoscience Frontiers*, 7, 315-334.
- 676 Song, W.L., Xu, C., Smith, M.P., Chakhmouradian, A.R., Brenna, M., Kynicky, J., Chen,
- 677 W., Yang, Y.H., Deng, M., and Tang, H.Y. (2018) Genesis of the world's largest rare
- 678 earth element deposit, Bayan Obo, China: Protracted mineralization evolution over
- 679 ~1 b.y. *Geology*, 46, 323-326.
- 680 Su, J.H., Zhao, X.F., Li, X.C., Hu, W., Chen, M., and Xiong, Y.L. (2019) Geological and
- 681 geochemical characteristics of the Miaoya syenitecarbonatite complex, Central
- 682 China: Implications for the origin of REE-Nb enriched carbonatite. *Ore Geology*
- 683 *Reviews*, 113, 103101.
- 684 Taylor, H.P., Frechen, J., and Degens, E.T. (1967) Oxygen and carbon isotope studies of
- 685 carbonatites from the Laacher See District, West Germany and the Alno District,
- 686 Sweden. *Geochimica et Cosmochimica Acta*, 31, 407-430.
- 687 Verplanck, P.L., Mariano, A.N., Mariano, A.J. (2016) Rare earth element ore geology of
- 688 carbonatites. *Reviews in Economic Geology*, 18, 5-32.
- 689 Williams-Jones, A.E., and Migdisov, A.A., (2014) Rare earth element transport and
- 690 deposition by hydrothermal fluids. *Acta Geologica Sinica (English Edition)*, 88,
- 691 472-474.
- 692 Williams-Jones, A.E., Migdisov, A.A., and Samson, I.M. (2012) Hydrothermal

693 mobilization of the rare earth elements – a tale of “Ceria” and “Yttria”. *Elements*, 8,
694 355-360.

695 Woolley, A.R., and Kjarsgaard, B.A. (2008) Paragenetic types of carbonatite as indicated
696 by the diversity and relative abundances of associated silicate rocks: evidence from a
697 global database. *The Canadian Mineralogist*, 46, 741-752.

698 Wu, Y.B., and Zheng, Y.F. (2013) Tectonic evolution of a composite collision orogen: an
699 overview on the Qinling–Tongbai–Hong’an–Dabie–Sulu orogenic belt in Central
700 China. *Gondwana Research*, 23, 1402-1428.

701 Xiao, B., Li, Q.G., He, S.Y., Chen, X., Liu, S.W., Wang, Z.Q., Xu, X.Y., and Chen, J.L.
702 (2017) Contrasting geochemical signatures between Upper Triassic Mo-hosting and
703 barren granitoids in the central segment of the South Qinling orogenic belt, central
704 China: Implications for Mo exploration. *Ore Geology Reviews*, 81, 518-534.

705 Xie, Y.L., Hou, Z.Q., Yin, S.P., Dominy, S.C., Xu, J.H., Tian, S.H., and Xu, W.Y. (2009)
706 Continuous carbonatitic melt-fluid evolution of a REE mineralization system:
707 Evidence from inclusions in the Maoniuping REE deposit, Western Sichuan, China.
708 *Ore Geology Reviews*, 36, 90-105.

709 Xu, C., Campbell, I.H., Allen, C.M., Chen, Y., Huang, Z., Qi, L., Zhang, G., and Yan, Z.
710 (2008) U–Pb zircon age, geochemical and isotopic characteristics of carbonatite and
711 syenite complexes from the Shaxiongdong, China. *Lithos*, 105, 118-128.

712 Xu, C., Kynicky, J., Chakhmouradian, A.N., Campbell, I.H., and Allen, C.M. (2010)
713 Trace-element modeling of the magmatic evolution of rare-earth-rich carbonatite

- 714 from the Miaoya deposit, central China. *Lithos*, 118, 145-155.
- 715 Xu, T.L., Ma, C.P., Lv, X.Z., and Liu, X.Y. (2012) Geological characteristics and
716 prospecting direction of Shejiayuan silver gold deposits in Yunxi Country, Hubei
717 Province. *Resources Environment and Engineering*, 26, 104-110.
- 718 Xu, C., Chakhmouradian, A.R., Taylor, R.N., Kynicky, J., Li, W.B., Song, W.L., and
719 Fletcher, I.R. (2014) Origin of carbonatites in the south Qinling orogen: implications
720 for crustal recycling and timing of collision between the south and North China
721 blocks. *Geochimica et Cosmochimica Acta*, 143, 189-206.
- 722 Xu, F., Li, W.B., Song, G.S., Wang, M.Z., Kang, Q.Q., Cao, Y., and Zhu, W.P. (2018)
723 Ore-controlling factors and metallogenic model of gold deposit in Shiquan-Xunyang
724 area, Shanxi. *Mineral Exploration*, 9, 70-78 (in Chinese).
- 725 Yang, X.Y., Lai, X.D., Pirajno, F., Liu, Y.L., Ling, M.X., and Sun, W.D. (2017) Genesis
726 of the Bayan Obo Fe-REE-Nb formation in Inner Mongolia, North China Craton: A
727 perspective review. *Precambrian Research*, 288, 39-71.
- 728 Yang, K.F., Fan, H.R., Pirajno, F., and Li, X.C. (2019) The Bayan Obo (China) giant
729 REE accumulation conundrum elucidated by intense magmatic differentiation of
730 carbonatite. *Geology*, 47, 1198-1202.
- 731 Ying, Y.C., Chen, W., Lu, J., Jiang, S.Y., and Yang, Y.H. (2017) In situ U-Th-Pb ages of
732 the Miaoya carbonatite complex in the South Qinling orogenic belt, Central China.
733 *Lithos*, 290, 159-171.
- 734 Ying, Y.C., Chen, W., Simonetti, A., Jiang, S.Y., and Zhao, K.D. (2020) Significance of

735 hydrothermal reworking for REE mineralization associated with carbonatite:
736 Constraints from in situ trace element and C-Sr isotope study of calcite and apatite
737 from the Miaoya carbonatite complex (China). *Geochimica et Cosmochimica Acta*,
738 280, 340-359.

739 Yuan, H.L., Gao, S., Dai, M.N., Zong, C.L., Gunther, D., Fontaine, G.H., Liu, X.M.,
740 Diwu, C. (2008) Simultaneous determinations of U - Pb age, Hf isotopes and trace
741 element compositions of zircon by excimer laser-ablation quadrupole and
742 multiple-collector ICPMS. *Chemical Geology*, 247, 100-118.

743 Yue, S.W., and Deng, X.H. (2019) Geological and ore-forming characteristics of Ag-Au
744 and polymetallic deposits in northwestern Hubei, China. *Earth Science Frontiers*,
745 26(6), 106-128 (in Chinese).

746 Yue, S.W., Zhai, Y.Y., Deng, X.H., Yu J.T., and Yang, L. (2013) Fluid inclusion and H-O
747 isotope geochemistry and ore genesis of the Yindonggou deposit, Zhushan County,
748 Hubei, China. *Acta Petrologica Sinica*, 29(1), 27-45 (in Chinese).

749 Zeng, L.P., Zhao, X.F., Li, X.C., Hu, H., and Mcfarlane, C. (2016) In situ elemental and
750 isotopic analysis of fluorapatite from the Taocun magnetite-apatite deposit, Eastern
751 China: Constraints on fluid metasomatism. *American Mineralogist*, 101, 2468-2483.

752 Zhang, C.L., Gao, S., Yuan, H.L., Zhang, G.W., Yan, Y.X., Luo, J.L., and Luo, J.H. (2007)
753 Sr-Nd-Pb isotopes of the early Paleozoic mafic-ultramafic dykes and basalts from
754 south Qinling belt and their implications for mantle composition. *Science China*
755 *Earth Science*, 50, 1293-1301.

756 Zhang, Y., Chen, Y.J., Qi, J.P., Leng, C.B., and Zhao, C.H. (2010) Geochemistry of
757 Gongguan-Qingtonggou Hg-Sb deposit in Xunyang, Shaanxi Province. *Acta*
758 *Mineralogica Sinica*, 30, 98-106 (in Chinese).

759 Zhang, W., Chen, W.T., Gao, J.F., Chen, H.K., and Li, J.H. (2019a) Two episodes of REE
760 mineralization in the Qinling Orogenic Belt, Central China: in-situ U-Th-Pb dating
761 of bastnäsite and monazite. *Mineralium Deposita*, 54, 1365-1280.

762 Zhang, D.X., Liu, Y., Pan, J.Q., Dai, T.G., and Bayless, R.C. (2019b) Mineralogical and
763 Geochemical Characteristics of the Miaoya REE Prospect, Qinling Orogenic Belt,
764 China: Insights from Sr-Nd-C-O Isotopes and LA-ICP-MS Mineral Chemistry. *Ore*
765 *Geology Reviews*, 110, 102932.

766 Zhu, J., Wang, L., Peng, S., Peng, L., Wu, C., and Qiu, X. (2016) U-Pb zircon age,
767 geochemical and isotopic characteristics of the Miaoya syenite and carbonatite
768 complex, Central China. *Geological Journal*, 52, 938-954.

769

770

771

772

FIGURE CAPTIONS

773 **Fig. 1** (a) Simplified tectonic map of China. (b) Geological sketch of the Qinling
774 Orogenic Belt and the location of the Miaoya and Shaxiongdong deposits (modified from
775 Zhang et al. 2019a). (c) Simplified geological map of the Miaoya complex (modified
776 from Liu et al., 1984). (d) Simplified geological map showing the distributions of various

777 REE ore bodies in the Miaoya complex (modified from Liu et al., 1984). Abbreviations:
778 S-NCB–Southern North China Block, NQL–North Qinling, SQL–South Qinling,
779 N-SCB–Northern South China Block.

780

781 **Fig. 2** Field photos and BSE images of various rocks/ores in the Miaoya complex. (a)
782 Carbonatites intruding syenites. (b) The boundaries between the carbonatites and syenites
783 are sharp/straight. Note that the syenites have been carbonatized. (c) Xenoliths of wall
784 rocks locally present in the carbonatites. (d) Veins of quartz + dolomite crosscutting
785 carbonatites. (e) Veins of ankerite + quartz in the carbonatite crosscut by stockworks
786 consisting of bastnäsite, pyrite and graphite. (f) Fine-grained syenite composed
787 dominantly of K-feldspar and albite with minor apatite. Note that the rock was
788 extensively altered. (g) Carbonatite is composed of calcite and apatite with minor
789 ilmenite and chlorite. (h) Veinlet of fluorite + bastnäsite crosscutting carbonatites. (i)
790 Veinlet of K-feldspar + albite + quartz + ankerite crosscutting carbonatites. Abbreviations:
791 Ab – albite, Ank – ankerite, Ap – apatite, Bas – bastnäsite, Cal – calcite, Chl – chlorite, Fl
792 – fluorite, Ilm – ilmenite, Kfs – K-feldspar, Ph – phengite, Py – pyrite, Qz – quartz, Sd –
793 siderite.

794

795 **Fig. 3** BSE images of diverse apatite grains in carbonatite and syenites and various REE
796 ores. (a) Euhedral to subhedral apatite grains in carbonatites are intergrown with calcite
797 and/or pyrite, eroded or replaced by phengite, K-feldspar, monazite, and quartz. (b) The

798 apatite in carbonatites is extensively embayed by dolomite, phengite, biotite, pyrite and
799 K-feldspar. Note that the apatite contains abundant monazite and bastnäsite inclusions. b1
800 is a CL image of this grain. (c) Apatite in the carbonatite is extensively modified and
801 contains three domains with irregular and sharp contacts. Note that BSE-dark-II domain
802 occurs as strips which embay both the BSE-bright and BSE-dark-I domains. (d) A
803 number of monazite grains distributed along the margins of modified apatite in the
804 carbonatites. (e) Relatively large monazite inclusions hosted in an extensively modified
805 apatite grain in the carbonatites. (f) Disseminated monazites in ferrocarbonatite are
806 irregular in shape, and homogenous under high-contrast BSE imagings (f1). (g)
807 Disseminated bastnäsite in carbonatite. Note that the bastnäsite is mainly associated with
808 the BSE-dark domains of the calcite. (h) Veinlet of bastnäsite + parisite + quartz in
809 carbonatites. (i) Veinlet of monazite + ankerite + graphite in syenite. (j) Veinlets of
810 batnäsite + allanite in carbonatite. (k) Abundant strontianite, barite, celestite and
811 bastnäsite grains mainly distributed in the BSE-dark areas in the calcite. (l) Veinlets of
812 barite + albite + apatite in syenite. Abbreviations: Brt – barite, Clt – celestite, Dol –
813 dolomite, Mnz – monazite, Par – parisite, Str – strontianite. Other abbreviations are the
814 same as those in Fig. 2.

815

816 **Fig. 4** Bimodal plots of F vs. LREE_2O_3 (a), REE+Y vs. Si (b), REE+Y vs. Na (c), Ca vs.
817 REE+Y+Na (d), REE+Y vs. Sr (e), Th+U vs. Pb (f), $(\text{La}/\text{Yb})_N$ vs. REE+Y (g), $(\text{La}/\text{Nd})_N$
818 vs. REE+Y (h), and LREE vs. HREE+Y (i) for different areas in the apatite.

819

820 **Fig. 5** Chondrite-normalized REE patterns from the BSE-bright (a), BSE-dark-I (b), and
821 BSE-dark-II (c) areas in the apatite.

822

823 **Fig. 6** Bimodal plots of Na vs. LREE (a), Fe+Mn+Mg vs. LREE (b), and (La/Yb)_N vs.
824 LREE (c) from different areas in the calcite.

825

826 **Fig. 7** Elemental mapping of an apatite grain from the carbonatites, showing the
827 distribution patterns of Ca, P, La, Sr, and F in the grain.

828

829 **Fig. 8** Plots of in-situ ⁸⁷Sr/⁸⁶Sr vs. ⁸⁸Sr (v) values from the the BSE-bright and BSE-dark I
830 and II areas in the apatite. Note that ⁸⁸Sr(v) represents the Sr signal intensities during
831 analyses.

832

833 **Fig. 9** Histograms showing ε_{Nd}(t=220 Ma) values for different areas in the apatite (a),
834 various monazites (b), and bastnäsite (c). Note: ε_{Nd}(t) values are calculated based on the
835 age of 220 Ma; ε_{Nd}(t) = [(¹⁴³Nd/¹⁴⁴Nd)_S(t) / (¹⁴³Nd/¹⁴⁴Nd)_{CHUR}(t) - 1] × 10000; where S =
836 sample, (¹⁴³Nd/¹⁴⁴Nd)_{CHUR} = 0.512638, (¹⁴⁷Sm/¹⁴⁴Nd)_{CHUR} = 0.1967.

837

838 **Fig. 10** Fluid inclusions in the altered apatite. (a) BSE image and (b) transmit-light image
839 of an altered apatite grain containing abundant fluid inclusions. Also note that small voids

840 are randomly distributed in the grain, possibly representing relics of fluid inclusions. (c)
841 Typical fluid inclusions composed of a liquid phase and vapor bubble. (d) Laser Raman
842 spectra collected at room temperature for the vapor bubble of the fluid inclusion, showing
843 that the bubbles are rich in CO₂. (e) Homogenization temperatures of the fluid inclusions.
844 Also shown are those in quartz from the 220-200 Ma orogenic Au-Ag deposits in the
845 South Qinling unit (data from Feng et al., 1997; Pang et al., 2001; Xu et al., 2012, 2018;
846 Yue et al., 2013). (f) Fluid inclusion salinities. Also shown are fluid inclusion salinities
847 from the orogenic Au-Ag deposits (data from Xu et al., 2012; Yue et al., 2013).
848 Abbreviations are the same as those in Fig. 2.

849

850 **Fig. 11** Calculated enrichment factors relative to Tm and Lu for various elements during
851 alteration of apatite (a) and calcite (b).

852

853 **Fig. 12** Summary of previous C-O isotopic compositions of carbonate grains from the
854 Miaoya complex (Xu et al., 2014; Cimen et al., 2018; Zhang et al., 2019b; Su et al.,
855 2019). The data for the orogenic Au-Ag deposits in South Qinling unit are cited from
856 Pang et al. (2001), Zhang et al. (2010), and Yue et al. (2019), whereas the field of primary,
857 mantle-derived carbonates is cited from Taylor et al. (1967). Arrows indicate
858 schematically the major processes responsible for changes in C-O isotopic compositions
859 (Demény et al., 1998).

860

861 **Fig. 13** Cartoons illustrating the formation process of the REE mineralization in the
862 Miaoya deposit. (a) The carbonatites and syenites in the Miaoya complex formed initially
863 at ca. 440-430 Ma, during which magmatic calcite, apatite, and minor allanite and
864 monazite formed. (b) Significant remobilization of early cumulated REEs in apatite and
865 calcite were triggered by the infiltration of external fluids at ca. 220 Ma, responsible for
866 the formation of abundant monazite and bastnäsite. (c) At the hydrothermal stage, the
867 early cumulated REEs were remobilized and transported on scales of meters or even
868 possibly tens of meters to be re-deposited as monazite and/or bastnäsite. Further details
869 are available in the text.

Fig. 1

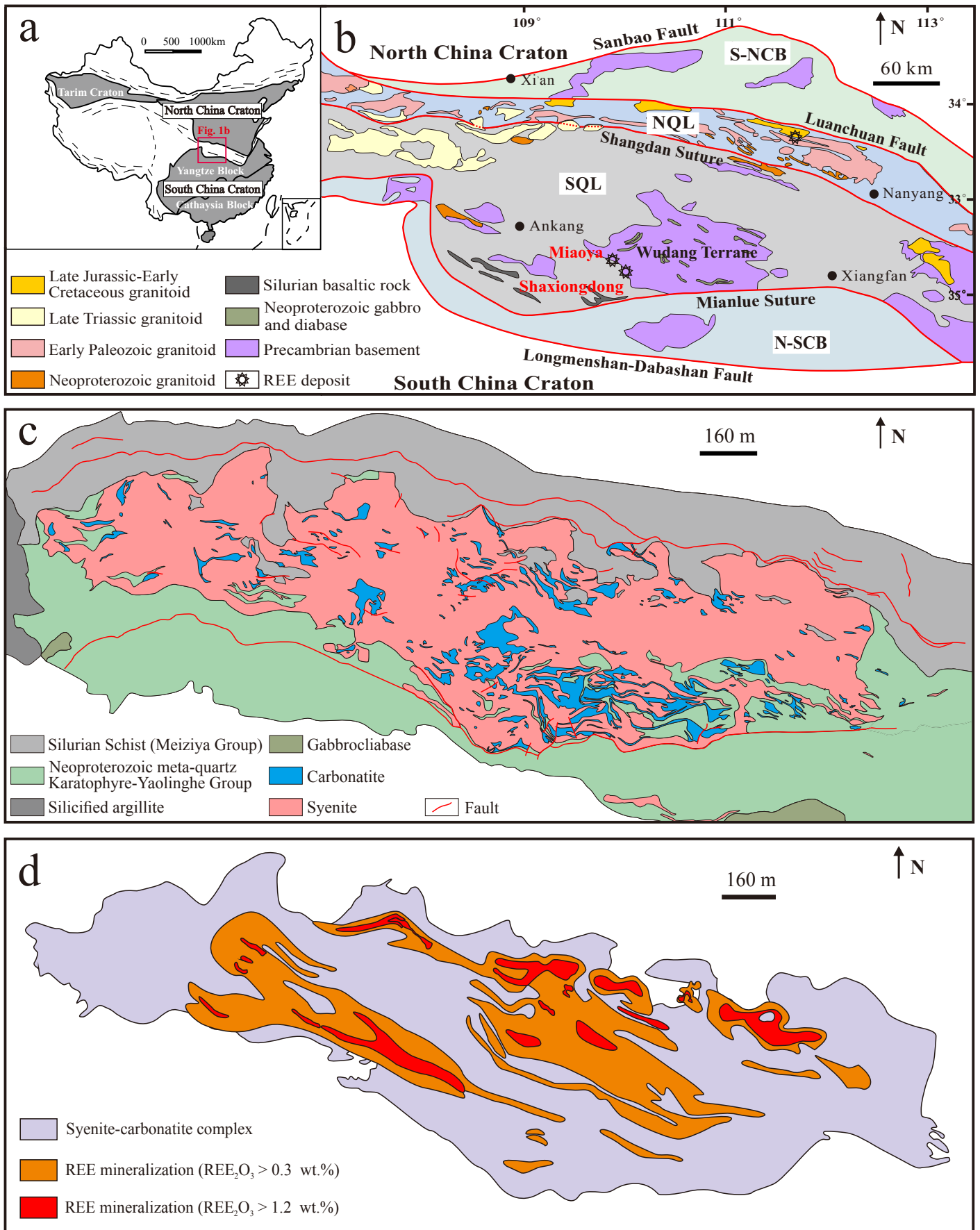


Fig. 2

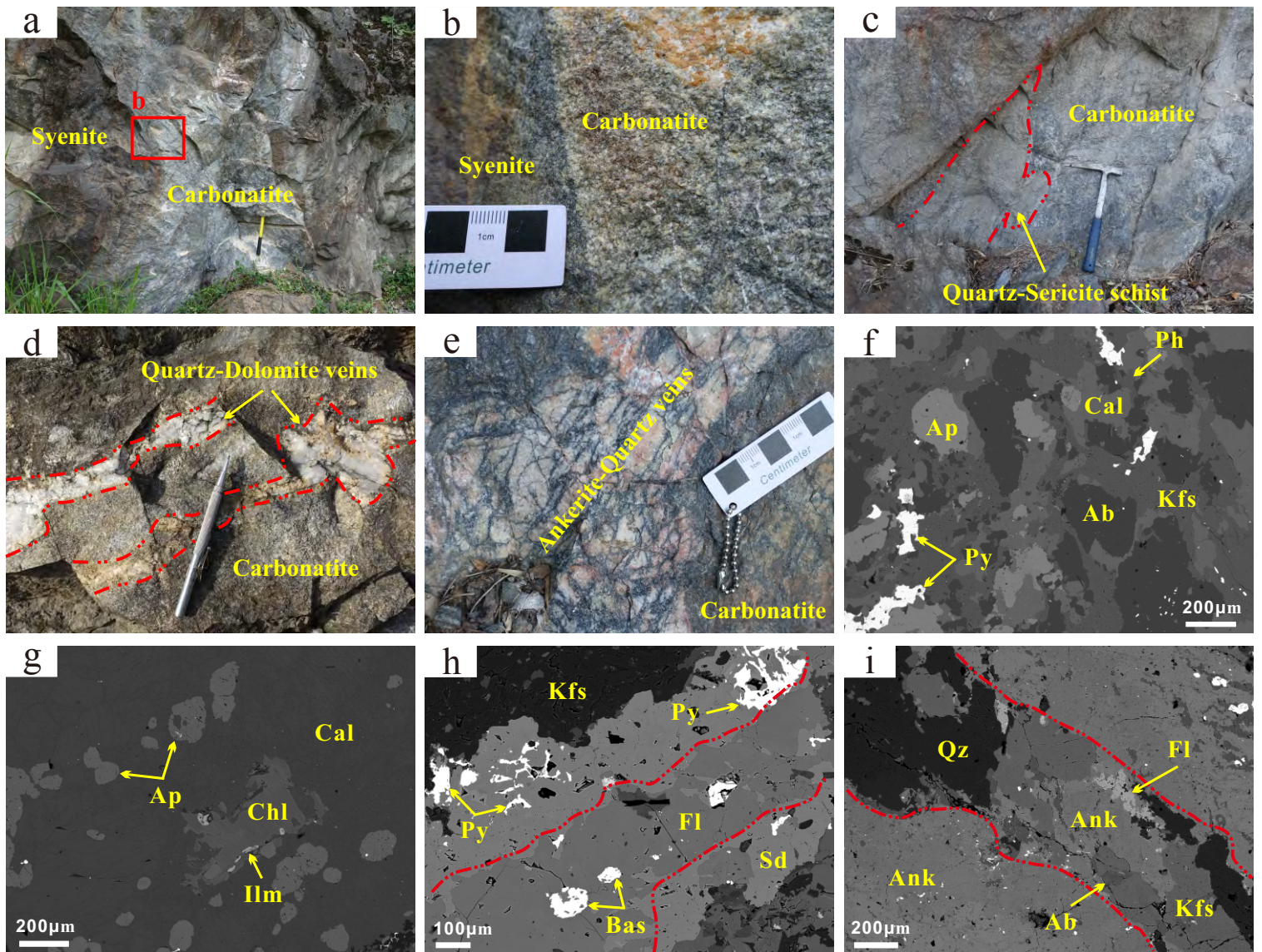


Fig. 3

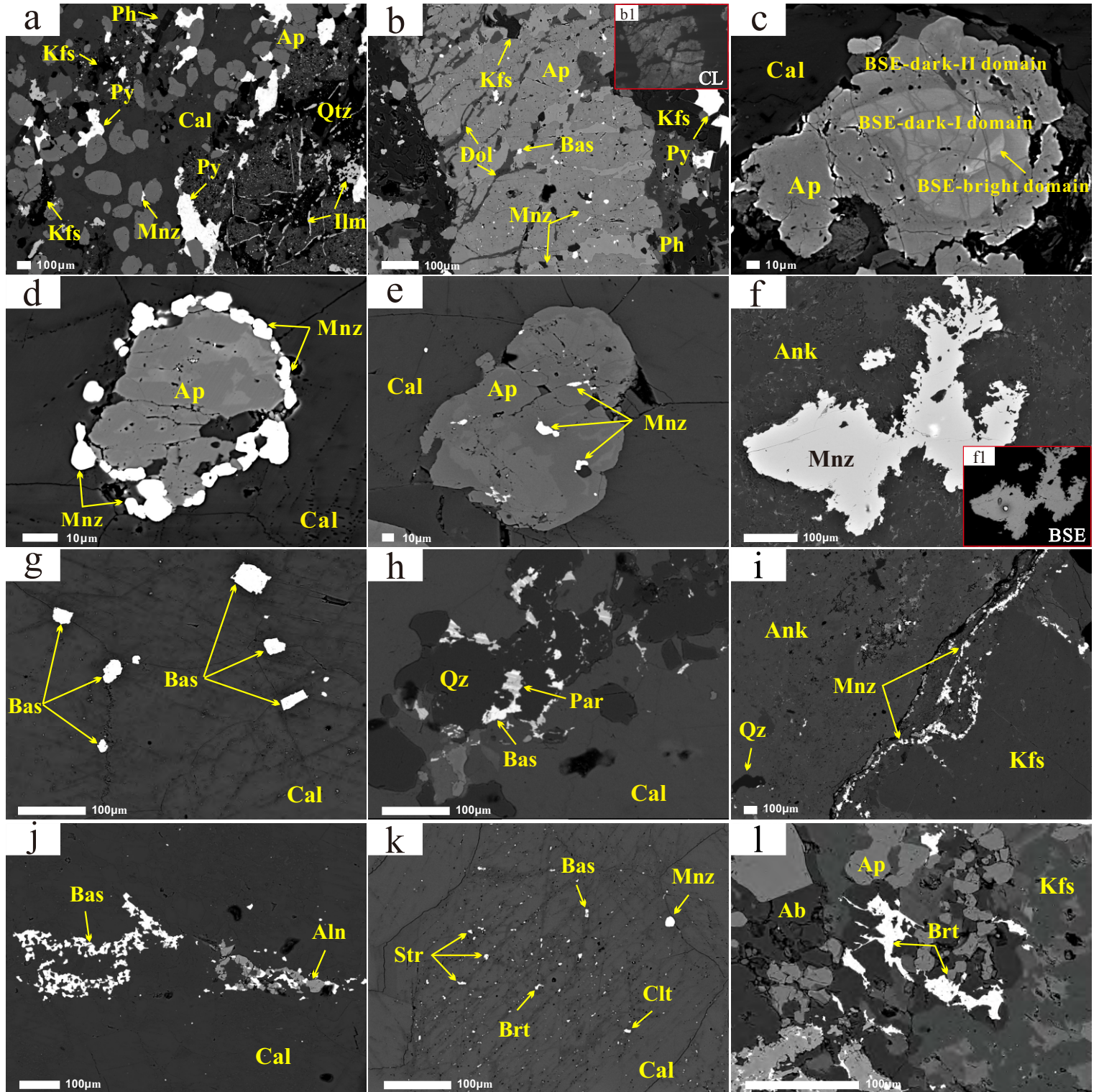


Fig. 4

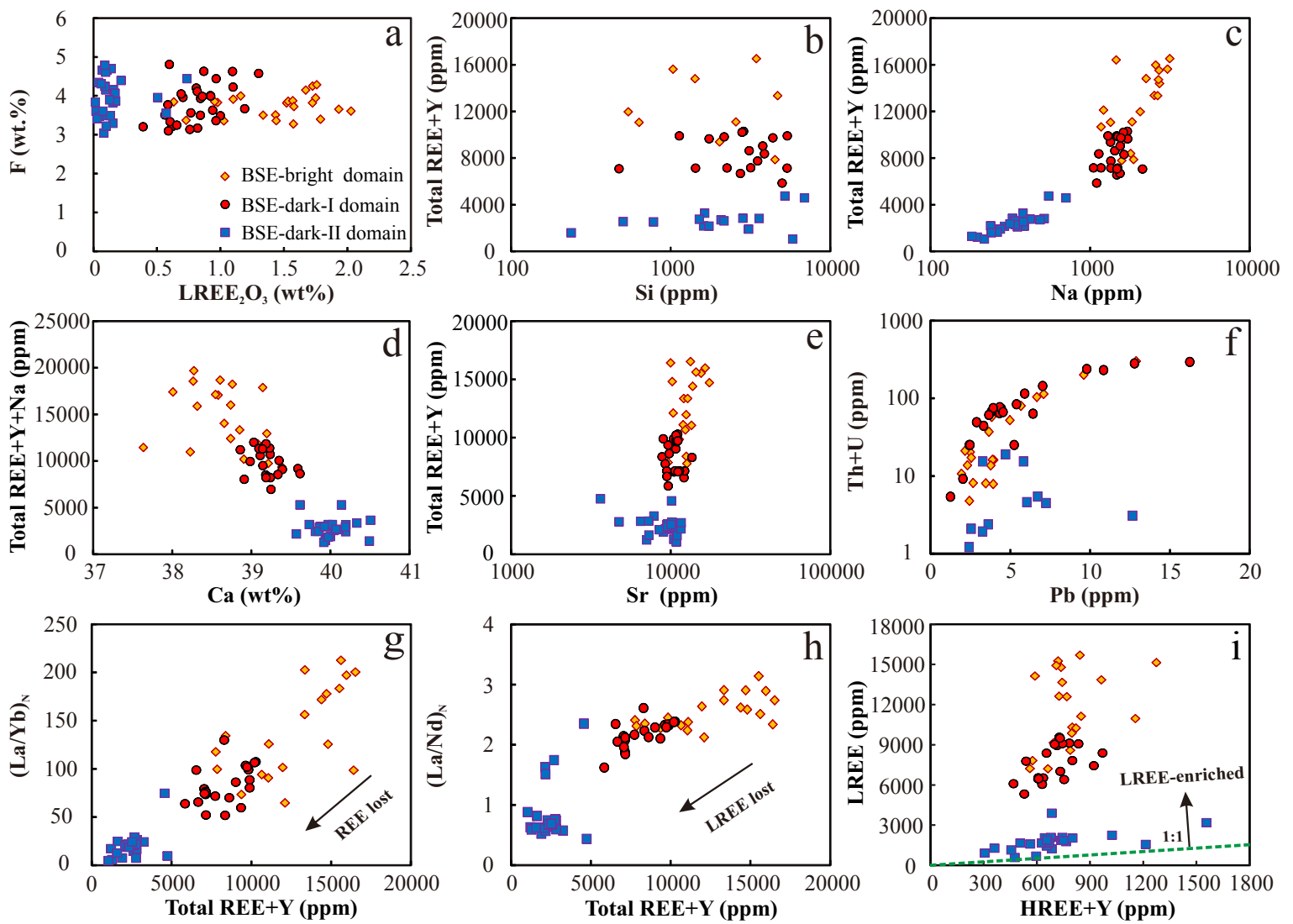


Fig. 5

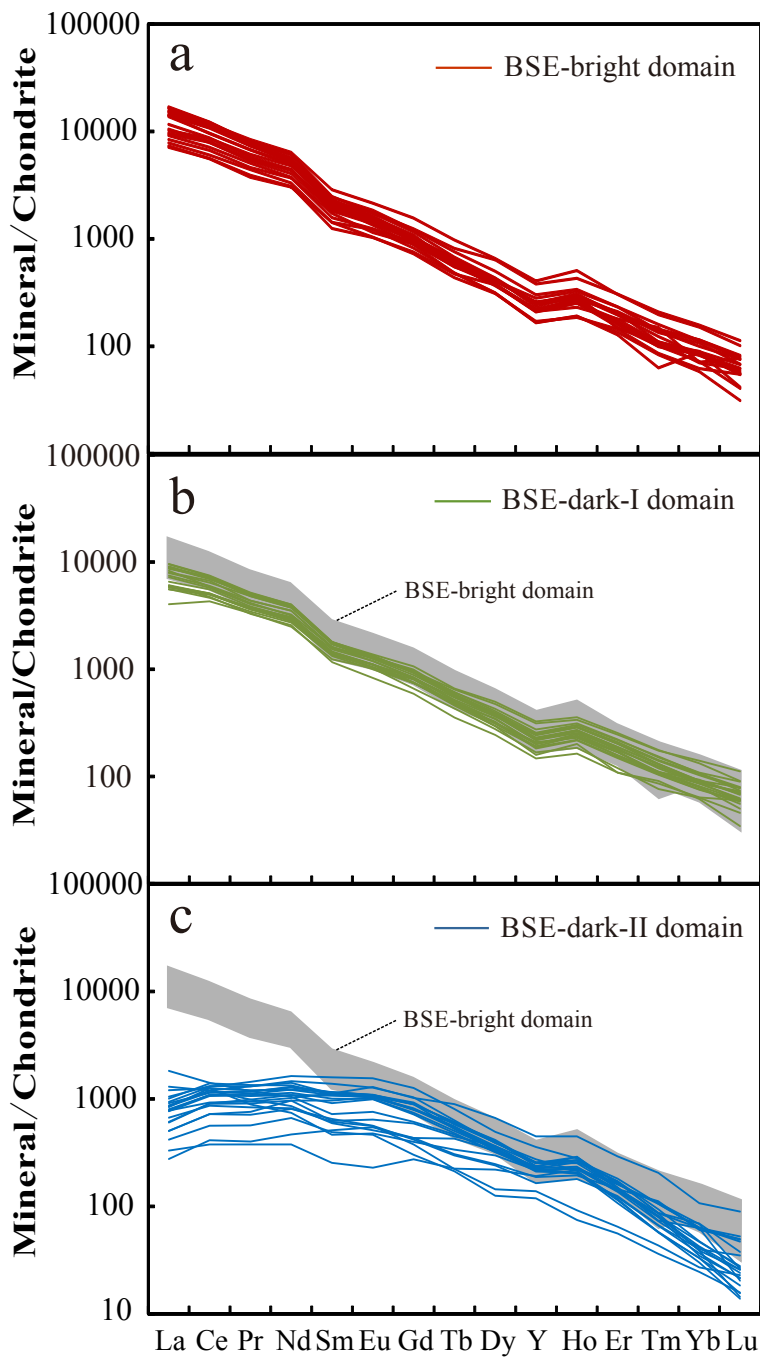


Fig. 6

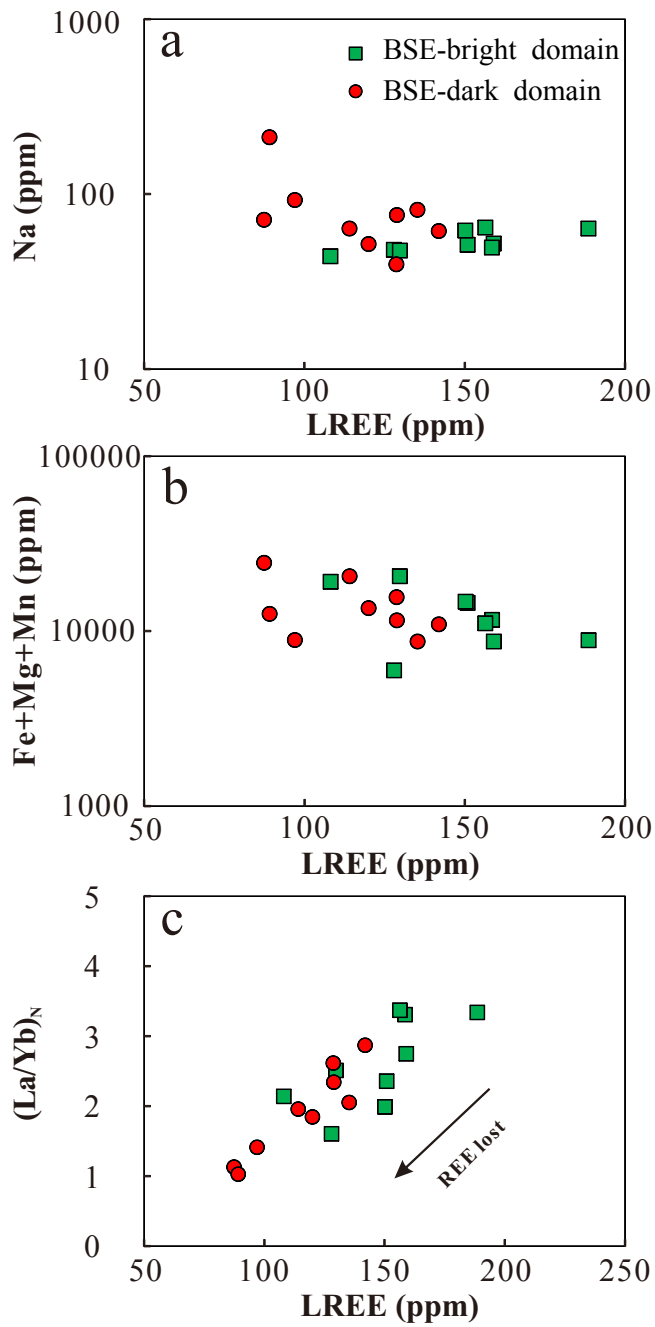


Fig. 7

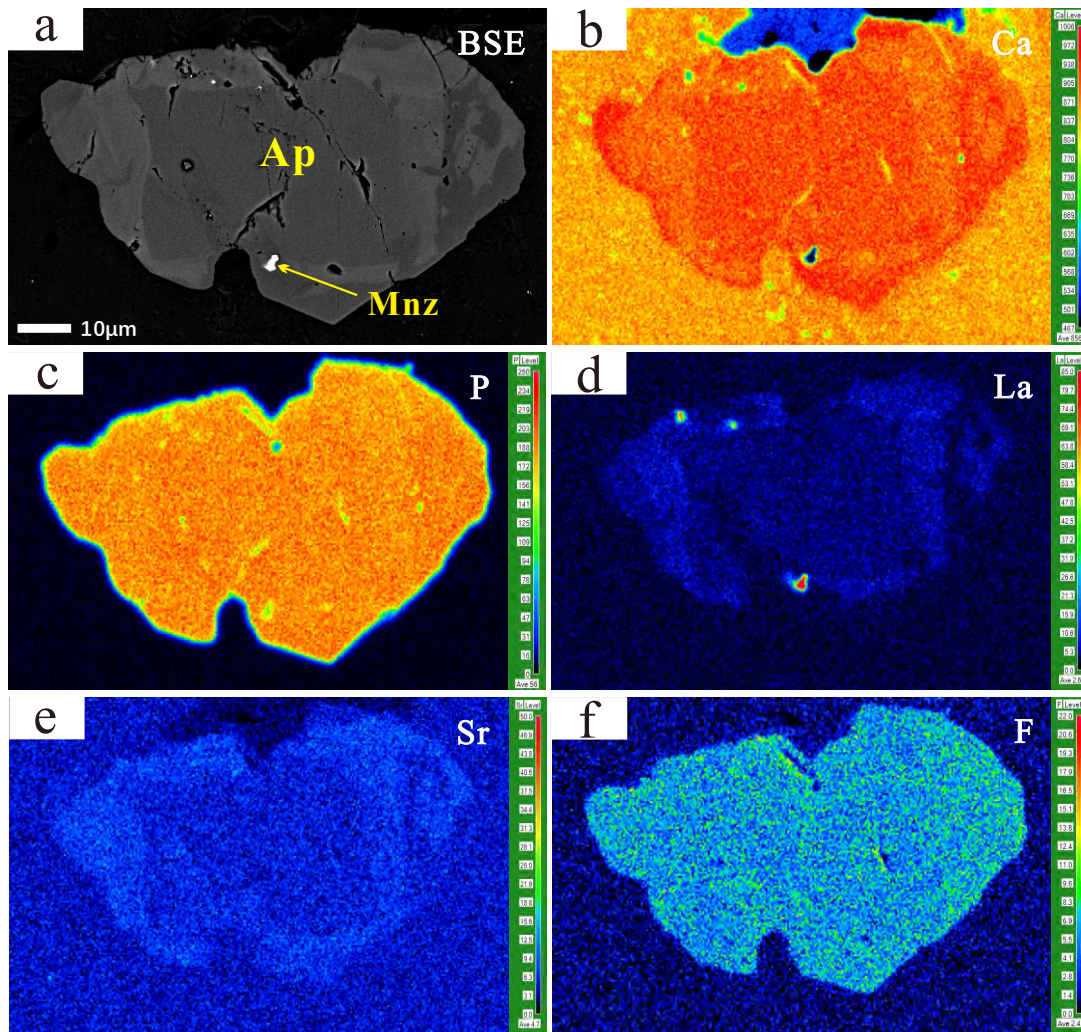


Fig. 8

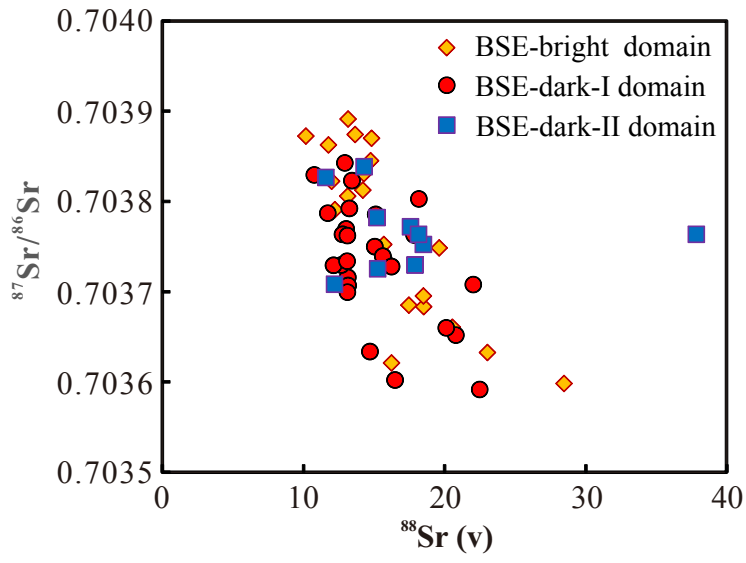


Fig. 9

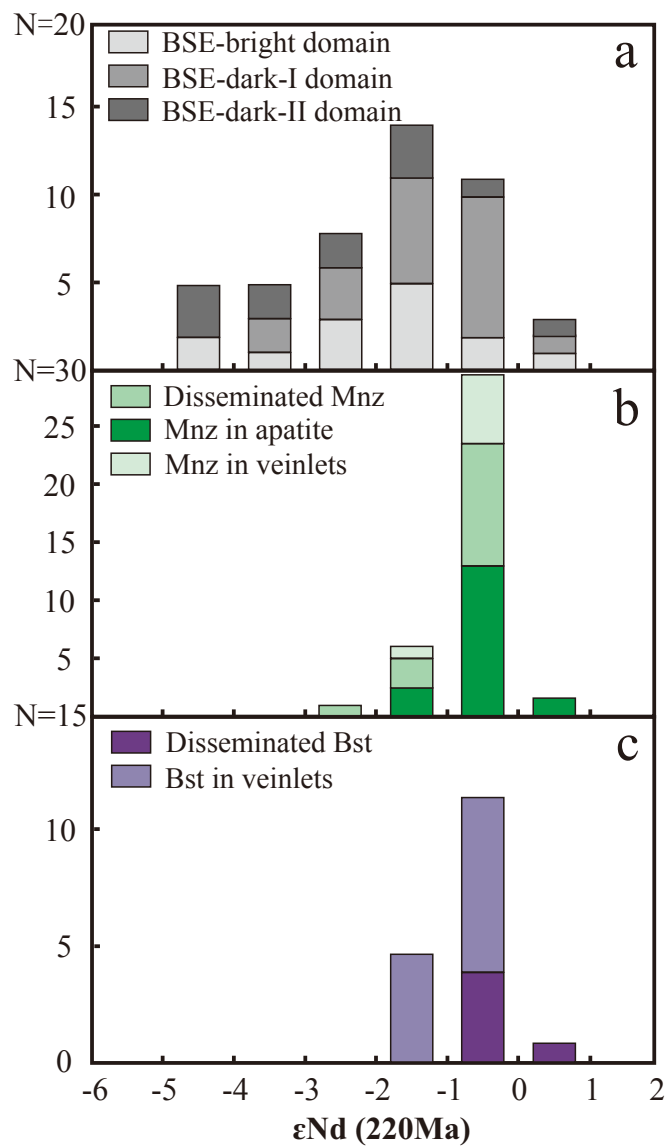


Fig. 10

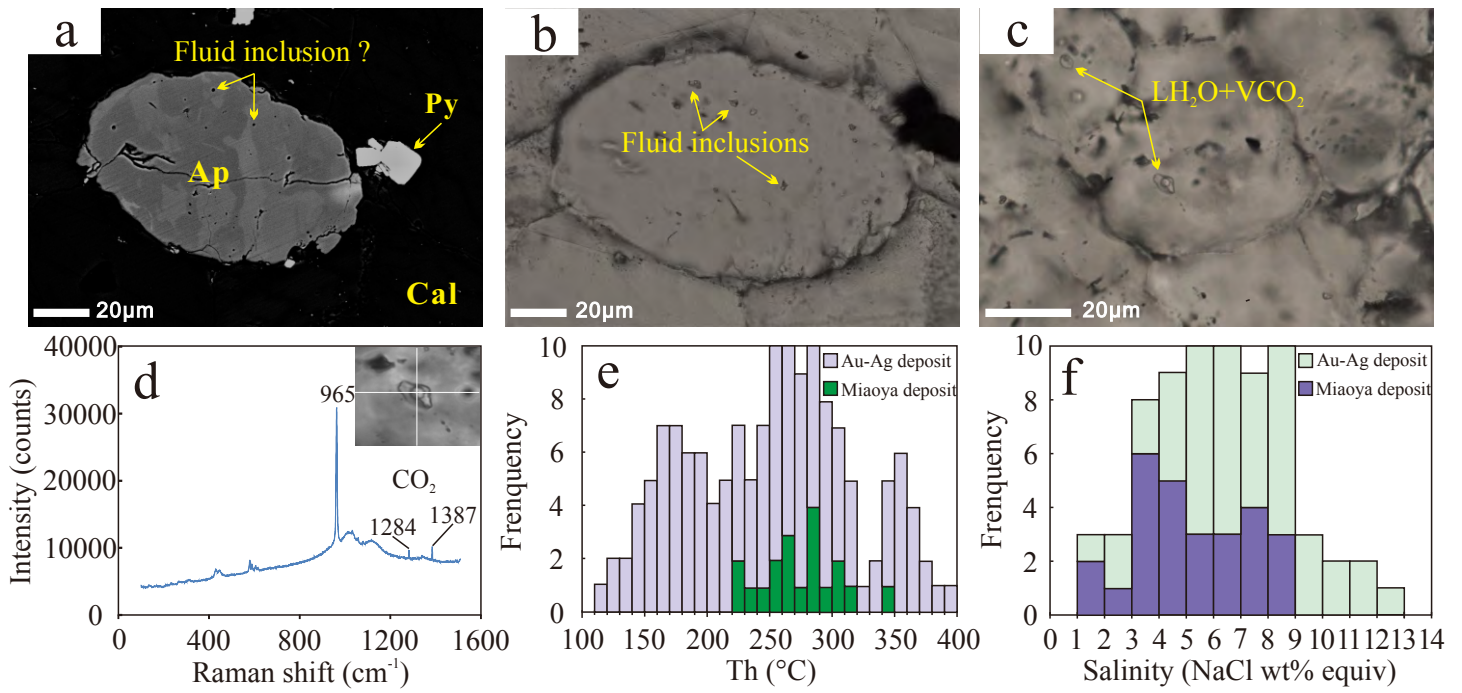


Fig. 11

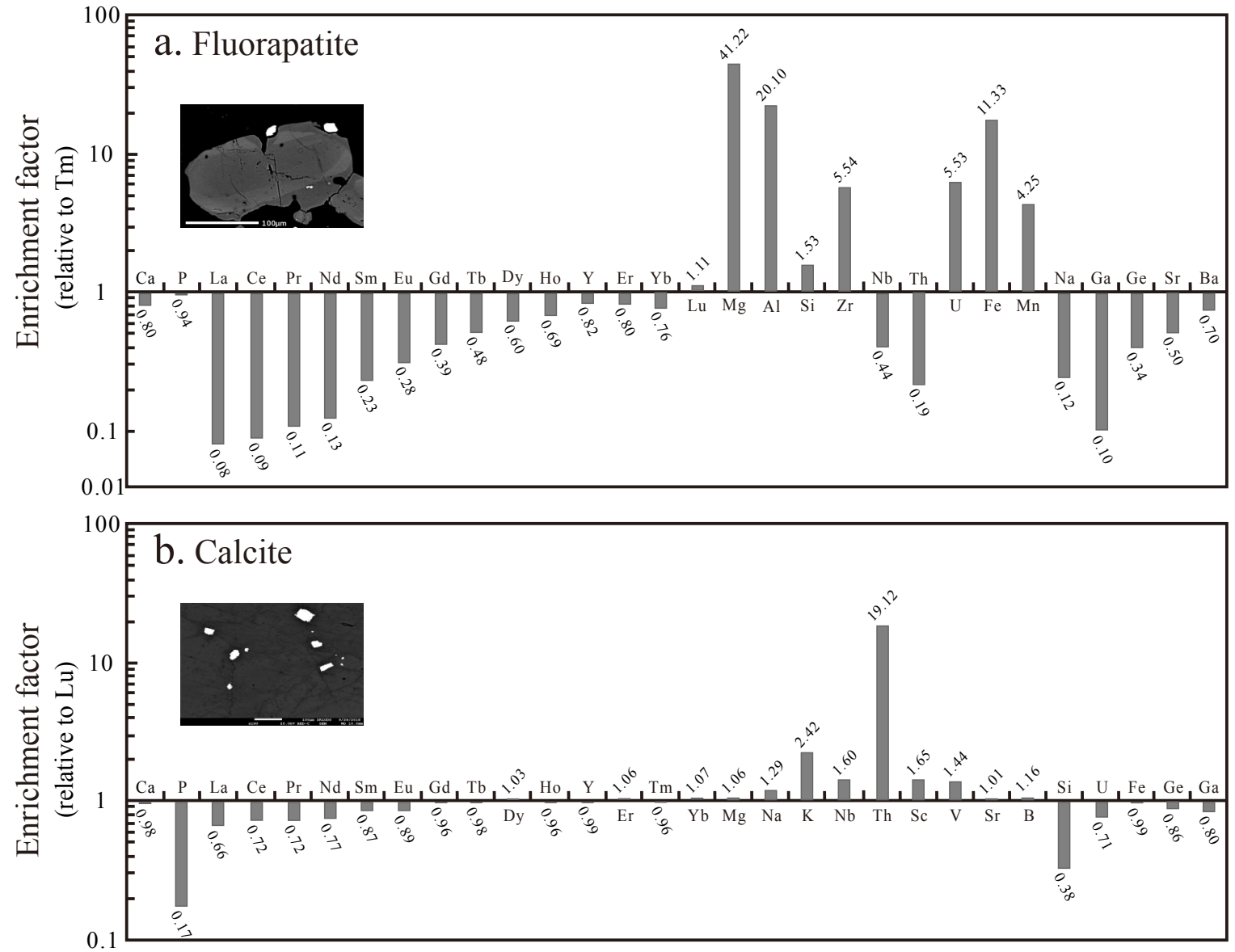


Fig. 12

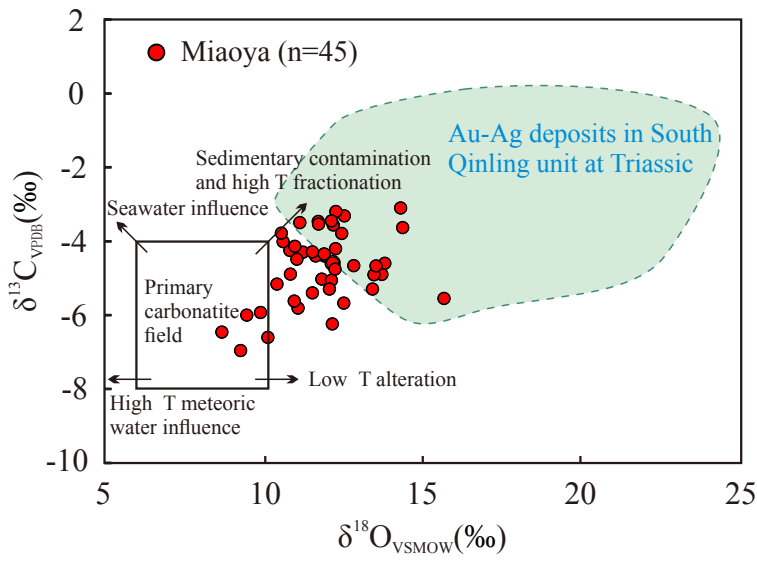


Fig. 13

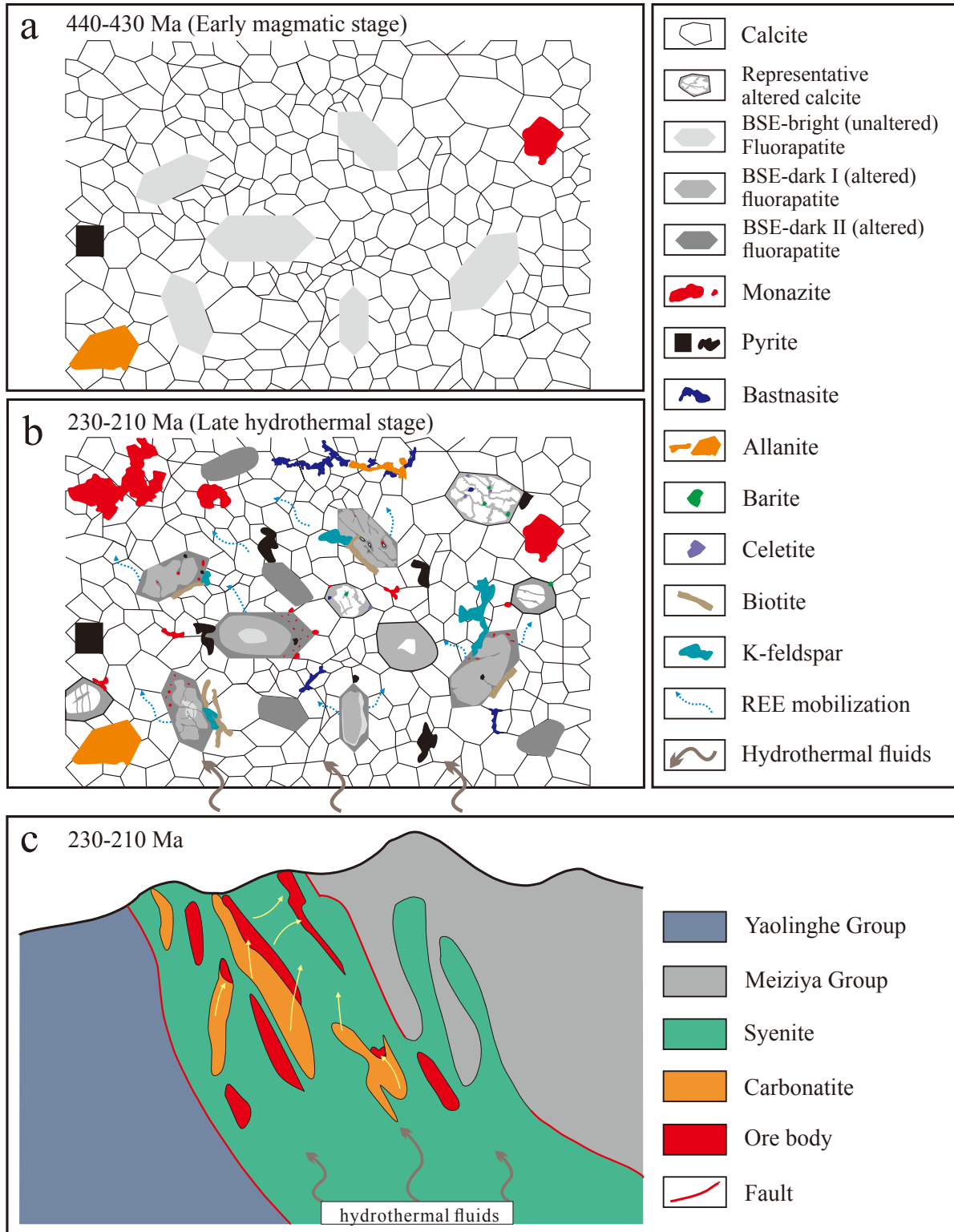


TABLE 1 Steps of the calculation related the total mobilized REEs from carbonatites and syenites

	Carbonatites	Syenites
Covering Area (m²)	4.9 × 10 ⁵	5.85 × 10 ⁶
Maximum depth (m)		640
Maximum volume (m³)	3.15 × 10 ⁸	3.76 × 10 ⁹
Average proportion of apatite	9.5%	1%
Average proportion of calcite	85%	12%
Maximum volume of apatite (m³)	2.99 × 10 ⁷	3.76 × 10 ⁷
Maximum volume of calcite (m³)	2.68 × 10 ⁸	4.51 × 10 ⁸
Remobilized amounts of LREE from apatite (Mt)	1.173	1.476
Remobilized amounts of LREE from calcite (Mt)	0.032	0.054
Remobilized amounts of LREE (Mt)	1.205	1.53
Total amount of remobilized LREE (Mt)		2.735

Note: The densities of fluorapatite and calcite are 3.19 ton/m³ and 2.71 ton/m³, respectively. Average LREE contents of fluorapatite and calcite are 13660 and 155 ppm, respectively. We have calculated that about 89.8% and 28.3% of LREEs (La, Ce, Pr, Nd) lost from the primary fluorapatite and calcite, respectively. Firstly, we need to calculate the maximum volume of carbonatites and syenites. Secondly, Maximum volume of apatite and calcite can be calculated based on the average proportion of apatite and calcite, and the maximum volume of carbonatites and syenites. Thirdly, remobilized amounts of LREEs from apatite and calcite can be calculated based on the densities, average LREE contents, estimated proportion of LREE losses and the maximum volume of apatite and calcite. Finally, the sum of the LREE remobilized from apatite and calcite in carbonatites and syenites represents total amount of remobilized LREEs.